PHYSICAL REVIEW D **82,** 054028 (2010)

Production-decay interferences at next-to-leading order in QCD for t-channel single-top-quark production

P. Falgari, P. Mellor, and A. Signer

IPPP, Department of Physics, University of Durham, Durham DH1 3LE, England

(Received 8 July 2010; published 24 September 2010)

We present a calculation of $\mathcal{O}(\alpha_s)$ contributions to the process of t-channel single-top production and decay, which include virtual and real corrections arising from the interference of the production and decay subprocesses. The calculation is organized as a simultaneous expansion of the matrix elements in the couplings $\alpha_{\rm ew}$, α_s and the virtuality of the intermediate top quark, $(p_t^2 - m_t^2)/m_t^2 \sim \Gamma_t/m_t$, and extends earlier results beyond the narrow-width approximation.

DOI: 10.1103/PhysRevD.82.054028 PACS numbers: 14.65.Ha

I. INTRODUCTION

Both the D0 and CDF Collaborations have recently announced the observation of single-top production at the Fermilab Tevatron at a significance of 5 standard deviations [1,2]. This process represents a promising channel for the study of the charged-current weak interactions of the top quark, and will play a prominent role in the physics program at the LHC, where top quarks will be produced singly at large rates. Measurements of the single-top production cross section can be used to directly determine V_{tb} and to test the unitarity of the CKM matrix [3]. Furthermore, angular correlations of the products of the top-quark decay encode information on the spin structure of the Wtb vertex and on the production dynamics of the top quark [4,5]. The single-top production cross section also probes the bottom-quark distribution inside the proton, which at the moment is computed from light-parton densities rather than extracted from data. Therefore, this reaction represents a means of directly constraining the heavy-quark content of the proton. Finally, single-top production constitutes a background to a number of possible new-physics processes, most notably some channels important for Higgs boson searches. In view of all these considerations, a precise theoretical description of single-top production in hadronic collisions is highly desirable.

In the standard model single-top production proceeds via three main hadronic channels, namely, t-channel production, $qb \to q't$ or $\bar{q}b \to \bar{q}'t$; s-channel production, $q\bar{q}' \to t\bar{b}$; and associated tW production, $bg \to W^- t$. At the Tevatron and at the LHC the t-channel production process has the largest cross section. In particular, at the LHC the s-channel production cross section and the tW production cross section are expected to be, respectively, 20 times and 3 times smaller than the t-channel process (see, e.g., Ref. [6]). Thus, in this paper we concentrate on the t-channel production mechanism. However, the distinction between t-channel and s-channel production is problematic beyond leading order (LO) and we will have to be more precise (in Sec. II) in describing how exactly we construct our observables and what we include in our calculation.

Top-quark production, or the production of any unstable heavy particle, can be treated in several ways. The most straightforward way is to treat the top as a stable particle and ignore its decay. In this context, the cross section for the t-channel single-top production to next-to-leading order (NLO) in QCD was computed in Refs. [7,8]. Later, a fully differential calculation was presented in Refs. [9,10]. NLO QCD corrections have also been computed for s-channel and associated tW production [9,11,12]. The full electroweak corrections in the standard model and MSSM were computed in Ref. [13] for stable t-channel single-top production, and very recently for both t- and s-channel processes [14]. Finally, effects of soft-gluon corrections beyond NLO have also been studied [15].

Beyond the stable-top approximation, the one-loop corrections split in a gauge-invariant way into so-called *factorizable* and *nonfactorizable* corrections [16,17]. Factorizable corrections correspond to (on-shell) corrections to either the production or the decay part of the process. Thus, a way to simplify the calculation is to separately compute the corrections to the production and decay of an on-shell top. This approximation (sometimes referred to as the improved narrow-width approximation) allows the inclusion of realistic cuts on the decay products of the top. NLO QCD analyses in this framework for the semileptonic top decay were published in Refs. [18–21].

To our knowledge, none of the currently published works on t-channel single-top production include the effects of interference between real radiation in production and decay or virtual corrections connecting the two subprocesses. A study of these nonfactorizable contributions has been presented for s-channel single-top production [22] and for $t\bar{t}$ production [23]. These corrections are known to be very small, for observables which are inclusive enough in the invariant mass of the top quark [24,25], due to large cancellations between virtual and real contributions. However, there is, *a priori*, no reason why this should hold true for arbitrary observables, especially if

they involve kinematical cuts that could, in principle, spoil the delicate cancellation of real and virtual contributions.

In this paper we want to assess the effect of these production-decay interferences in t-channel single-top production at NLO in the QCD coupling constant, α_s. Hence, we are interested in resonant top-quark production with $p_t^2 \neq m_t^2$, but $p_t^2 \simeq m_t^2$ or, more precisely, $p_t^2 - m_t^2 \sim m_t\Gamma_t$, where $\Gamma_t \simeq 1.4$ GeV is the width of the top. While the effect of these ''off-shell'' corrections is expected to be very modest for the total cross section, we are particularly interested in distributions that are related to the measurement of the top-quark mass, m_t. For a reliable mass determination with an error $\delta m_t < \Gamma_t$, the nonfactorizable corrections have to be under control. In this respect, we also view the current calculation as a preparation to apply our method to top-quark pair production.

We will neglect quark-mixing effects and treat the bottom quark as massless throughout, using the 5-flavor scheme. The importance of bottom-quark mass corrections and the relation between the 4-flavor and 5-flavor scheme has been studied in Refs. [26,27]. Furthermore, our calculation does not include any effects due to parton showers. The matching of the NLO QCD result with parton shower Monte Carlo was implemented in MC@NLO [28] and in POWHEG [29].

The calculation is organized as an expansion in the virtuality of the top quark, $p_t^2 - m_t^2$, in a way similar to the pole approximation [30,31], and employs effective-theory (ET) inspired techniques analogous to the ones used in Refs. [32–34]. These are based on splitting contributions to the amplitude into so-called hard and soft parts using the method of regions [35,36], thereby extending the separation between factorizable and nonfactorizable corrections beyond NLO. The hard part can be identified with the factorizable corrections, whereas the soft part corresponds to the nonfactorizable contributions [37]. This approach has the advantage of providing a gauge-invariant resummation of top-quark finite-width effects. Furthermore, the expansion in $p_t^2 - m_t^2$ allows for an identification of the terms relevant to the achievement of a given target accuracy before the actual computation, leading to a significant simplification of the calculation. The method has been discussed in detail for a toy model [33] and can easily be adapted to our case for the tree-level and virtual contributions. For the real corrections this is more problematic and we will not be able to follow a strict ET approach in this case, but will have to combine ideas from the effective theory with a standard fixed-order approach. As will be shown in this paper, this results in straightforward calculations of the contributions that are expected to be relevant for phenomenological applications at hadron colliders.

The outline of the paper is as follows: we start with a general description of our method to deal with resonant particles at hadron colliders in Sec. II. While we will concentrate on the process at hand, the discussion is meant to be general enough to be easily adapted to other processes. We will also be more precise in describing the observables we are interested in and the accuracy we are aiming for. In Sec. III we first give explicit results for the amplitudes needed and details of the computation. We then discuss a series of successive approximations to the exact cross section, which relate to previous results in the literature, and illustrate the cancellation of infrared singularities in the various cases. Numerical results for the cross sections and distributions will be presented in Sec. IV. Finally, in Sec. V we summarize and give an outlook on further possible applications of our method.

II. METHOD

A. Setup of the calculation

In order to include production-decay interference effects, the narrow-width approximation has to be relaxed. In particular, the top quark cannot be treated as a stable particle. Physical observables must be computed for final states containing only long-enough lived particles, which in the case of interest in this paper are represented by the products of the top-quark decay. Considering the LHC, we are interested in the process

$$p(P_1)p(P_2) \to J_b(p_b)W^+(p_W)X, \tag{2.1}$$

where J_b is a b-quark jet and X stands for an arbitrary number of further jets, as long as they do not originate from a b or $\bar{b}$ quark. Rejecting $\bar{b}$-quark jets (naively) excludes contributions from the s-channel process. Furthermore, we do not allow a second W in the final state in order to exclude associated production, and we insist on a positively charged lepton (from the W decay) to exclude single-$\bar{t}$ production. Some of these constraints are, of course, questionable from an experimental point of view and most could easily be avoided. But this is a minimal, more or less realistic setup that allows us to discuss the inclusion of nonfactorizable corrections.

The most important constraint we make on the final state is that the invariant mass of the W^+J_b pair is close to the top-quark mass, i.e., that the top is resonant. More precisely, we require[1] $(p_b + p_W)^2 - m_t^2 \sim m_t\Gamma_t \sim \alpha_{\rm ew} m_t^2 \ll m_t^2$. As is well known, in this case strict fixed-order perturbation theory breaks down due to the kinematic enhancement of formally higher-order corrections. These corrections have to be resummed in a consistent way.

To illustrate this, consider the process (2.1) at partonic tree level, where we have to compute

$$\begin{aligned} q(p_1)b(p_2) &\to q'(p_3)b(p_4)W^+(p_W) \\ &\to q'(p_3)b(p_4)l^+(p_5)\nu_l(p_6), \end{aligned} \tag{2.2}$$

[1]If taken at face value this would correspond to an invariant-mass window $\Delta p_t \sim \Gamma_t$ around the top-quark mass. In fact, a numerical study reveals that the suppression of nonresonant configurations is already effective for much looser invariant-mass cuts.

with the initial parton, q, being a light quark (u, c) or antiquark ($\bar{d}, \bar{s}$). Accordingly, q' is either a quark (d, s) or antiquark ($\bar{u}, \bar{c}$), respectively. For the purpose of the current discussion the b quark can be identified with a b jet, J_b, with momentum $p_b = p_4$. The decay of the $W^+ \to l^+ \nu_l$ is described in the improved narrow-width approximation. This considerably simplifies the calculation, and yet allows for a noninclusive treatment of the leptons coming from the W-boson decay.

The matrix element for the partonic process (2.2) can be computed from the Feynman diagrams shown in Fig. 1. These can be divided into two classes: *resonant diagrams* [(diagram 1(a)], in which the Wb pair originates from the decay of an internal top-quark; and *nonresonant* or *background diagrams* [(diagrams 1(b) and 1(c); and diagrams 1(d)–1(f)], that do not contain intermediate top-quark lines. The latter are subdivided into electroweak-mediated [(diagrams 1(d)–1(f)] and mixed QCD-EW diagrams [(diagrams 1(b) and 1(c)]. It is important to note that only the sum of all electroweak diagrams [(diagram 1(a); and diagrams 1(d)–1(f)] is gauge invariant, though, strictly speaking, only diagram 1(a) describes the production of a single top quark. Obviously, the sum of all QCD-EW diagrams is separately gauge independent.

The fixed-order tree-level amplitude, $\mathcal{A}^{\text{tree}}$, can be written as

$$\mathcal{A}^{\text{tree}} = \frac{\mathcal{K}(p_i)}{p_t^2 - m_t^2} + \mathcal{J}(p_i), \tag{2.3}$$

where $\mathcal{K}(p_i)$ and $\mathcal{J}(p_i)$ are functions of the external momenta, p_i, $i = 1, \ldots, 6$. The first term in Eq. (2.3) describes resonant contributions, whereas $\mathcal{J}$ accounts for nonresonant diagrams. Equation (2.3) has a pole at $p_t^2 = m_t^2$ that is related to the breakdown of the fixed-order perturbation theory mentioned above. When an intermediate virtual top quark approaches the mass shell, a subset of formally subleading corrections to the top-quark propagator are enhanced, and must be resummed to all orders:

$$\frac{i(\not{p}_t + m_t)}{p_t^2 - m_t^2} \to \frac{i(\not{p}_t + m_t)}{p_t^2 - m_t^2} \sum_{n=0}^{\infty} \left[-i\bar{\Sigma}_t(\not{p}_t) \frac{i(\not{p}_t + m_t)}{p_t^2 - m_t^2} \right]^n. \tag{2.4}$$

$\bar{\Sigma}_t(\not{p}_t)$ denotes the sum of (renormalized) one-particle irreducible corrections to the top-quark two-point function, and contains an imaginary part of order $\alpha_{\text{ew}} m_t$ that, upon resummation, regularizes the propagator. However, mixing different orders in perturbation theory leads, in general, to a violation of gauge invariance and unitarity, which are guaranteed only for strictly fixed-order calculations and for the full amplitude. Therefore, a meaningful gauge-invariant expansion of the matrix element in $p_t^2 - m_t^2$

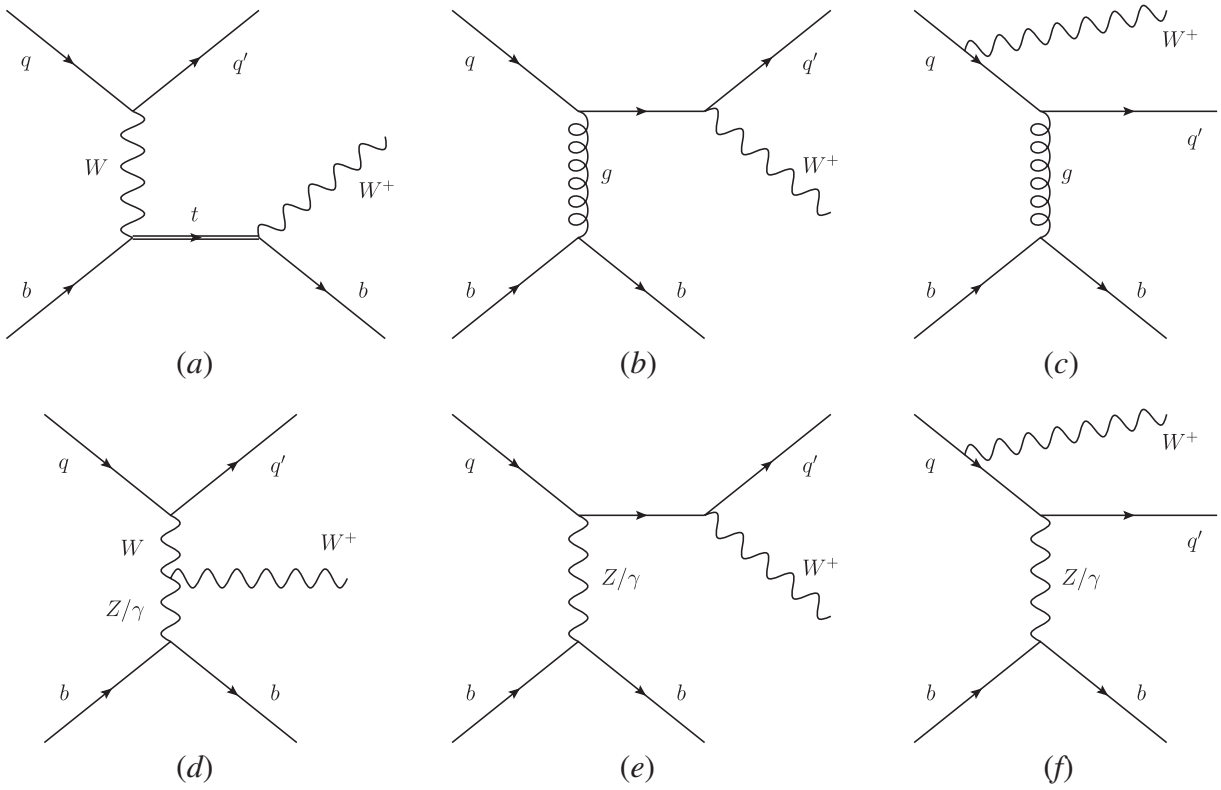

FIG. 1. Tree-level Feynman diagrams for the process $qb \to q'bW$. The figure shows both purely EW contributions, diagram 1(a) and diagrams 1(d)–1(f), and mixed QCD-EW contributions, diagrams 1(b) and 1(c). The semileptonic (on-shell) decay of the W is understood.

requires addressing the issue of resummation of finite-width effects.

In recent years, several frameworks for the gauge-invariant calculation of production cross sections for unstable particles have been proposed, from *ad hoc* procedures to treat weak gauge bosons [38], to more general methods based on complex renormalization [39,40] or modified perturbative expansion in terms of distributions [41–43]. Here we adopt an effective-theory inspired approach [33] which, in this case, can be considered as an extension of the pole-approximation scheme [30,31]. As we will see, this provides a consistent framework for a systematic gauge-invariant expansion of the amplitude around the complex pole of the full top propagator at $\mu_t^2 \equiv m_t^2 - i m_t \Gamma_t$. Note that we have used the same notation, m_t, for the mass parameter in Eq. (2.4) and for the real part of the complex pole. Strictly speaking, the first one is the scheme-dependent renormalized mass, $m_{t,r}$, and the latter the physical pole mass,[2] and in a generic renormalization scheme they differ by an amount proportional to α_s, as shown in Sec. III C. However, in the on-shell scheme adopted in this paper, the two masses coincide up to corrections which are beyond our target accuracy. Therefore, in the following we refrain from introducing more than one mass parameter, except for Sec. III C, where it will be necessary to explicitly distinguish the renormalized mass, $m_{t,r}$, from the pole mass, m_t.

For the tree-level amplitude, Eq. (2.3), the pole expansion reads

$$\mathcal{A}^{\text{tree}} = \frac{\mathcal{K}(p_i; p_t^2 = \mu_t^2)}{\Delta_t}(1 + \delta R_t) + \frac{\partial \mathcal{K}}{\partial p_t^2}(p_i, p_t^2 = \mu_t^2) + \mathcal{J}(p_i; p_t^2 = \mu_t^2) + \ldots, \tag{2.5}$$

where we have introduced $\Delta_t \equiv p_t^2 - \mu_t^2$, and $1 + \delta R_t$ denotes the residue of the full propagator at $p_t^2 = \mu_t^2$. The leading resonant contribution is encoded in $\mathcal{K}(p_i; p_t^2 = \mu_t^2)$. In $\partial \mathcal{K}/\partial p_t^2$ the resonant propagator has been cancelled by a Δ_t arising from the expansion of $\mathcal{K}(p_i)$ around $p_t^2 = \mu_t^2$, while $\mathcal{J}(p_i; p_t^2 = \mu_t^2)$ represents the leading contribution of the truly nonresonant diagrams. The ellipsis denotes higher-order contributions suppressed by additional powers of Δ_t. These can, in principle, be computed to any order, but in the following discussion only the terms shown in Eq. (2.5) will be relevant.

Beyond the leading approximation, $\mathcal{A}^{\text{tree}} \sim \mathcal{K}(p_i; p_t^2 = \mu_t^2)/\Delta_t$, the consistency of the expansion (2.5) requires the inclusion of loop corrections. The kinematic expansion in the parameter, Δ_t, must be combined with a standard expansion in the coupling constants, $\alpha_s = g_s^2/(4\pi)$ and $\alpha_{\text{ew}} = g_{\text{ew}}^2/(4\pi)$. For counting purposes, in the following we refer to the three expansions parameters collectively as δ and assume the relative scaling:

$$\delta \sim \alpha_s^2 \sim \alpha_{\text{ew}} \sim \frac{\Delta_t}{m_t^2}. \tag{2.6}$$

We are thus led to write the tree-level amplitude for the process (2.2) as

$$\mathcal{A}^{\text{tree}} = \delta_{31}\delta_{42}(g_{\text{ew}}^3 A_{(-1)}^{(3,0)} + g_{\text{ew}}^3 A_{(0)}^{(3,0)} + \ldots) + T_{31}^a T_{42}^a g_{\text{ew}} g_s^2 A^{(1,2)}. \tag{2.7}$$

The superscripts denote the order of the couplings which multiply the amplitude, while the subscripts denote the order to which the propagator, Δ_t, appears within the amplitude, i.e., $A_{(l)}^{(m,n)}$ has a prefactor $g_{\text{ew}}^m g_s^n$ with $A_{(l)}^{(m,n)} \sim \Delta_t^l$. The coupling from the decay of the W is not counted. A missing subscript indicates that the amplitude does not contain a Δ_t propagator, i.e., $A^{(m,n)} \equiv A_{(0)}^{(m,n)}$. Thus, $g_{\text{ew}}^3 A_{(-1)}^{(3,0)} \sim \delta^{1/2}$, $g_{\text{ew}} g_s^2 A^{(1,2)} \sim \delta$, and $g_{\text{ew}}^3 A_{(0)}^{(3,0)} \sim \delta^{3/2}$. Terms suppressed beyond $\delta^{3/2}$ are indicated by the ellipsis. In the notation of Eq. (2.5), $g_{\text{ew}}^3 A_{(-1)}^{(3,0)}$ corresponds to $\mathcal{K}(p_i; p_t^2 = \mu_t^2)/\Delta_t$, while $g_{\text{ew}}^3 A_{(0)}^{(3,0)}$ includes both the $\partial \mathcal{K}/\partial p_t^2$ and $\mathcal{J}$ terms. Clearly, $g_{\text{ew}} g_s^2 A^{(1,2)}$ receives contributions from nonresonant diagrams only.

Note that the QCD-EW contribution, $A^{(1,2)}$, is usually considered to be a background to single-top production. However, the final state is identical and, therefore, $A^{(1,2)}$ has to be included in $\mathcal{A}^{\text{tree}}$. In principle, there could be interferences between $A_{(-1)}^{(3,0)}$ and $A^{(1,2)}$, however, due to color they vanish at tree level. For the color-averaged squared amplitude, $M^{\text{tree}} = \frac{1}{N_c^2}\sum_c |\mathcal{A}^{\text{tree}}|^2$, we obtain

$$M^{\text{tree}} = g_{\text{ew}}^6 |A_{(-1)}^{(3,0)}|^2 + g_{\text{ew}}^6 2\,\text{Re}(A_{(-1)}^{(3,0)}[A_{(0)}^{(3,0)}]^*) + g_{\text{ew}}^2 g_s^4 \frac{C_F}{2N_c}|A^{(1,2)}|^2 + \ldots, \tag{2.8}$$

where, as usual, $N_c = 3$ and $C_F = 4/3$. The (first) leading term of Eq. (2.8) scales as δ, whereas the other two terms scale as δ^2 and represent a correction of order $\delta \sim 1\%$ to the leading contribution. All other terms are further suppressed.

Our aim is to compute all contributions to the cross section up to $\mathcal{O}(\delta^{3/2})$. According to our counting, Eq. (2.6), this requires, beside the leading tree-level amplitude, the calculation of $A_{(-1)}^{(3,2)}$, the $\mathcal{O}(\alpha_s)$ one-loop corrections to the leading resonant contribution. For the squared amplitude this leads to a contribution

$$M^{\text{NLO}} = g_{\text{ew}}^6 g_s^2 2\,\text{Re}(A_{(-1)}^{(3,2)}[A_{(-1)}^{(3,0)}]^*), \tag{2.9}$$

which we will refer to as NLO. Along with the virtual corrections we also have to include real corrections, $qb \to q' b W^+ g$. There are also gluon-initiated processes at NLO, namely $gb \to q' b W^+ \bar{q}$ and $qg \to q' b W^+ \bar{b}$. The former is

[2] It is well known that for a mass determination with an error $\delta m_t \lesssim \Lambda_{\text{QCD}}$, a mass definition other than the pole mass has to be used [44,45]. However, in this paper we ignore effects of the order $\Lambda_{\text{QCD}} \ll m_t \delta$.

fully included in our calculation, whereas the latter deserves special discussion as it mixes t-channel and s-channel single-top production. Writing the amplitude for $q(p_1)g(p_2) \to q'(p_3)b(p_4)W^+(p_W)\bar{b}(p_7)$ as

$$\mathcal{A}_{qg}^{\text{tree}} = g_s g_{\text{ew}}^3 (T_{47}^{a_2}\delta_{31}A_{qg}^{47} + T_{31}^{a_2}\delta_{47}A_{qg}^{31}), \tag{2.10}$$

we first note that upon squaring $\mathcal{A}_{qg}^{\text{tree}}$ there are no interference terms, due to color. Conventionally, the term $\sim|A_{qg}^{47}|^2$ is included in t-channel single-top production, whereas the term $\sim|A_{qg}^{31}|^2$ is considered to be a higher-order correction to s-channel single-top production. We will follow this convention but stress that a fully satisfactory solution requires the simultaneous inclusion of both processes, which we reserve for future work.

In summary, we need to compute the tree-level amplitudes for

$$ub \to dbW^+, \qquad \bar{d}b \to \bar{u}bW^+, \tag{2.11}$$

$$ub \to dbW^+g, \qquad \bar{d}b \to \bar{u}bW^+g, \tag{2.12}$$

$$ug \to dbW^+\bar{b}, \qquad \bar{d}g \to \bar{u}bW^+\bar{b}, \tag{2.13}$$

$$gb \to dbW^+\bar{u}, \tag{2.14}$$

and the QCD one-loop corrections to the leading (in Δ_t/m_t) part of process (2.11). Of course, we will also have to include the processes with $\{u, d\} \to \{c, s\}$. Note that the various processes containing a gluon are related by crossing. We stress once more that the semileptonic decay, $W^+ \to \ell^+\nu_\ell$, is taken into account in the improved narrow-width approximation.

B. Loop corrections in the effective-theory approach

Detailed discussions and applications of effective-theory methods to the calculation of processes involving unstable particles can be found in the literature [32,33,37,46]. Here we will restrict ourselves to a discussion of the points directly relevant to our calculation.

The main idea of the ET approach is to systematically exploit the hierarchy of scales, $(p_t^2 - m_t^2) \sim m_t\Gamma_t \ll m_t^2$, by integrating out degrees of freedom with virtuality $\sim m_t^2$. In doing this, the Lagrangian of the underlying theory is rewritten as a series of gauge-invariant operators multiplied by matching coefficients, which are determined such that the ET reproduces the results of the underlying theory up to a certain approximation. The matching coefficients are guaranteed to be gauge independent and they contain the information on the degrees of freedom that have been integrated out.

Once the hard part is integrated out, we are left with degrees of freedom with virtuality much smaller than m_t^2. In general, we have to take into account several different such degrees of freedom, but in the case at hand it is sufficient (to the accuracy we are aiming at) to consider only soft modes.

Within this picture, the leading contribution to the process (2.2) is to be viewed as the production of an on-shell top, the propagation of a soft top, and the subsequent decay of an on-shell top. This is to say that the matching of the full theory onto the ET is done on-shell. It is important to note that on-shell in this context means $p_t^2 = \mu_t^2$, i.e., on the complex pole of the two-point function. Thus, the matching coefficients are generally complex. The propagator of the soft top is derived from the bilinear operator in the effective theory and includes the resummation of the self-energy insertions.

There are several sources of higher-order corrections. First, there are $\mathcal{O}(\alpha_s)$ and $\mathcal{O}(\alpha_{\text{ew}})$ corrections to the matching coefficients. These correspond to loop corrections to the production and decay of a stable top and have been taken into account in previous calculations. Furthermore, there are subleading corrections to the bilinear operator, i.e., corrections to the propagator. There are also subleading operators in the ET that do not refer to a top quark at all. These operators reproduce the effect of background diagrams, as well as subleading effects of resonant diagrams, and correspond to the terms $\mathcal{J}$ and $\partial\mathcal{K}/\partial p_t^2$ in Eq. (2.5), respectively. Finally, there are the contributions from loop diagrams in the effective theory, i.e., loop diagrams with the still dynamical soft degrees of freedom. These contributions correspond to the nonfactorizable corrections and link the production and decay parts of the process.

From a technical point of view, the calculation of the aforementioned corrections is achieved by using the method of regions [35,36] and computing the hard and soft parts of loop integrals. The hard part is defined by expanding the integrand under the assumption that the loop momentum, q^μ, scales as $q \sim m_t$. In what follows we will always suppress powers of m_t in the scaling relations and write the scaling of the hard modes as $q^\mu \sim 1$. The soft part is obtained by expanding the integrand of a loop integral assuming that the loop momentum scales as $q \sim \delta$.

A strict application of the effective theory would require the introduction of collinear fields for the massless external fermions and a heavy-quark field for the top quark, as well as soft and collinear gauge-boson fields. However, we refrain from doing this because for the real corrections we will have to deviate from a strict ET approach anyway. We will, however, make extensive use of the gauge-invariant separation of the one-loop contribution into hard and soft parts, and the associated counting rules to obtain a result that is gauge invariant and reproduces all terms to the desired accuracy with a minimal amount of computation.

The one-loop diagrams necessary to achieving $\mathcal{O}(\delta^{3/2})$ accuracy are shown in Fig. 2. Apart from the top self-energy insertion [(diagram 2(b)], at the accuracy we are interested in we have to deal with QCD one-loop diagrams only. Because of color, the one-loop diagrams containing gluon exchange between the upper and lower quark lines

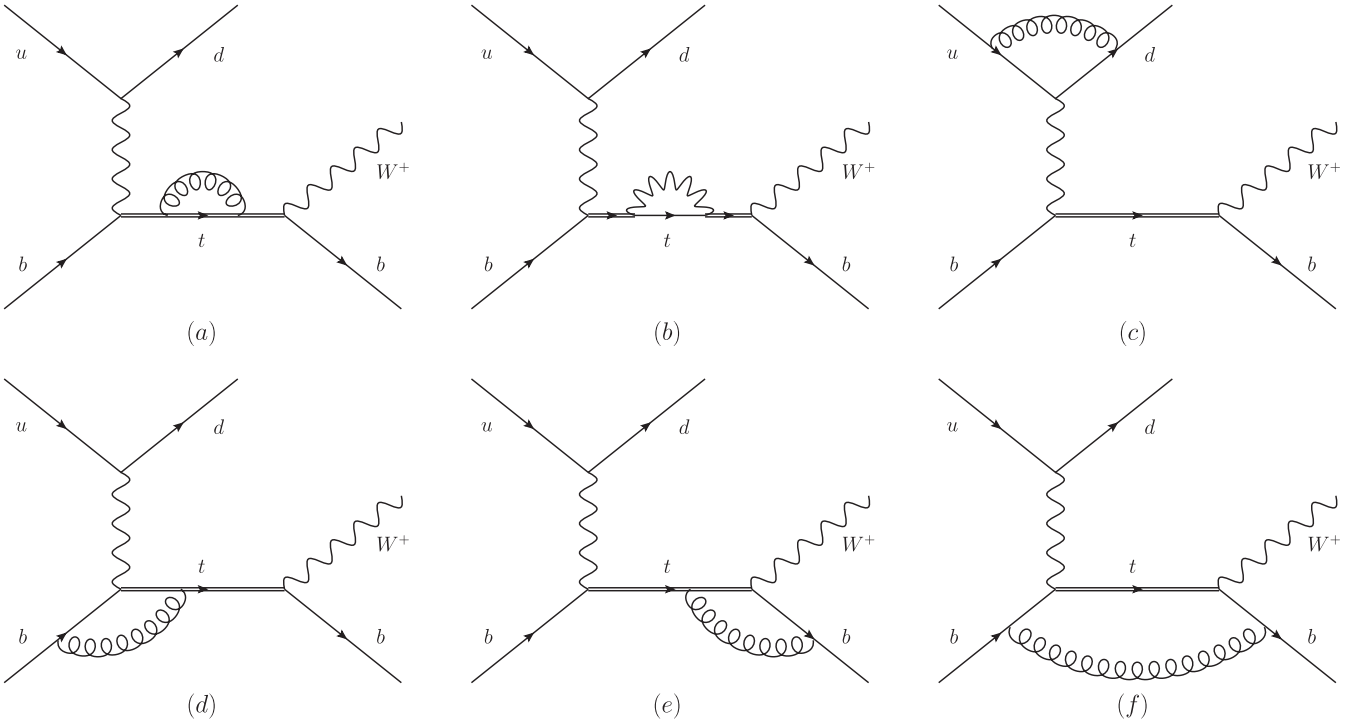

FIG. 2. Virtual QCD corrections to t-channel single-top production at leading order in Δ_t/m_t.

result in a vanishing contribution to the amplitude squared and are therefore not shown in the figure. A detailed discussion of the computation of the various diagrams will be given in Sec. III B. Here we briefly mention which parts of the diagrams in Fig. 2 enter our calculation.

As explained in detail in Sec. III B, taking the leading hard and soft parts of the QCD self-energy insertion [(diagram 2(a)] we obtain the scalings $g_{\mathrm{ew}}^3\alpha_s\delta^{-2} \sim 1$ and $g_{\mathrm{ew}}^3\alpha_s\delta^{-1} \sim \delta$, respectively. For the soft part this corresponds precisely to a correction we are interested in. The hard part, however, seems to be superleading, i.e., the one-loop correction is enhanced compared to the tree-level amplitude (which scales as $g_{\mathrm{ew}}^3/\delta \sim \delta^{1/2}$). However, as we will see below, in the on-shell scheme used in this paper this superleading contribution is cancelled precisely by the counterterm. In a generic renormalization scheme this is not the case, and the leading hard part of the self-energy has to be resummed and enters the definition of the complex pole, μ_t^2, as explained in detail in Sec. III C. The same applies to the two-loop QCD self-energy. An insertion of the leading hard part results in a diagram scaling as $g_{\mathrm{ew}}^3\alpha_s^2\delta^{-2} \sim \delta^{1/2}$ and, in general, has to be resummed. The subleading hard terms are suppressed by at least one factor $p_t^2 - m_t^2 \sim \delta$ compared to the leading hard contribution and, therefore, result in contributions $g_{\mathrm{ew}}^3\alpha_s\delta^{-1} \sim \delta$, i.e., of the same order as the leading soft contribution. Thus, the subleading hard part of the self-energy diagram has to be included (but not necessarily resummed) independent of the renormalization scheme adopted.

To obtain the scaling of the EW one-loop self-energy insertion we simply have to replace α_s by α_{ew}. Thus, diagram 2(b) scales as $\delta^{1/2}$ and $\delta^{3/2}$ with hard and soft EW self-energy insertions, respectively. Therefore, the hard part is not suppressed with respect to the tree-level amplitude and has to be resummed. The soft part contributes beyond the accuracy of our calculation and can be neglected. Obviously, the resummation of the hard part of the EW self-energy insertion corresponds to the resummation indicated in Eq. (2.4).

For diagram 2(c), the decomposition into hard and soft part is trivial in that the soft part results in scaleless integrals and therefore vanishes, whereas the hard part corresponds to the full diagram. This is not surprising as the loop correction in this diagram is not affected by the instability of the top quark.

Diagrams 2(d) and 2(e) are more interesting and both behave in a similar way. The soft and hard parts scale as $g_{\mathrm{ew}}^3\alpha_s\delta^{-1} \sim \delta$ and contribute at NLO. From an ET point of view, the hard part of diagram 2(d) contributes to the matching coefficient of the production operator [or to the decay operator in the case of diagram 2(e)], whereas the soft part is reproduced by a loop diagram in the effective theory.

Finally, performing a similar expansion for the box diagram [2(f)], it can be seen that the hard part scales as δ^2 and thus contributes beyond the accuracy of our calculation. The soft part, however, scales as δ and must be included at NLO. This illustrates the simplifications that can be achieved in the calculation. Rather than having to

compute a full box diagram with several scales, we end up computing only the soft part, which is much simpler.

C. Real corrections

For the tree-level and virtual calculations, an ET approach can be used in a straightforward manner. If one is only interested in the total cross section, real corrections can also be tackled in this way by relating the total cross section to the imaginary part of the forward-scattering amplitude. However, here we are interested in computing an arbitrary infrared-safe observable. Hence, we want to compute the real corrections without explicitly specifying the observable.

It is clear that, to a certain extent, this is in conflict with an ET approach. An effective theory relies on making all scales explicit. Since the definition of the observable itself can introduce additional scales, it is not possible to follow a strict ET approach. In this subsection we describe how we deal with the real corrections, making sure that we keep all terms to the desired accuracy, for a general observable. The only assumption we make on the observable is that it does not introduce another hierarchy of scales. We stress that this assumption has to be made for any fixed-order calculation because a large ratio of scales usually introduces large logarithms which have to be resummed.

To begin with, we need the real matrix element squared for the process (2.12). We show the diagrams containing a top-quark propagator in Fig. 3. There are additional diagrams corresponding to the diagrams [1(b)–1(f)] of Fig. 1 with an additional gluon radiated off, however, they are suppressed and contribute only beyond the accuracy we are aiming at. The real corrections have an additional factor of α_s, which allows us to work at leading order in Δ_t/m_t.

In the case of the real corrections it is not, *a priori*, clear what the correct expansion parameter is. Diagrams 3(a)–3(c) have a resonant-top propagator for $(p_W + p_4)^2 \simeq m_t^2$, diagram 3(e) has a resonant-top propagator for $(p_W + p_4 + p_g)^2 \simeq m_t^2$, and diagram 3(d) is resonant in both kinematic configurations. Depending on how the final state partons are combined to jets, both regions can be relevant and have to be taken into account. This can be achieved by a slight modification of the usual subtraction method.

In order to isolate infrared singularities, real corrections are usually computed by subtracting from the real, $n+1$ parton matrix element squared, M_{n+1}, a term $M^{\text{sing}}_{n(+1)}$ that approximates the full matrix element in all singular regions. This term has essentially n-parton kinematics. It is added back and a partial phase-space integration is performed analytically to recover the infrared $1/\epsilon$ poles explicitly. The kinematic configurations associated with $M^{\text{sing}}_{n(+1)}$ correspond either to a gluon being soft or two partons being collinear. Thus, for $M^{\text{sing}}_{n(+1)}$ it is always clear whether the gluon is combined with the b quark or not and, correspondingly, what the appropriate expansion parameter is. Therefore, we can expand the term that is added back and write for the real corrections

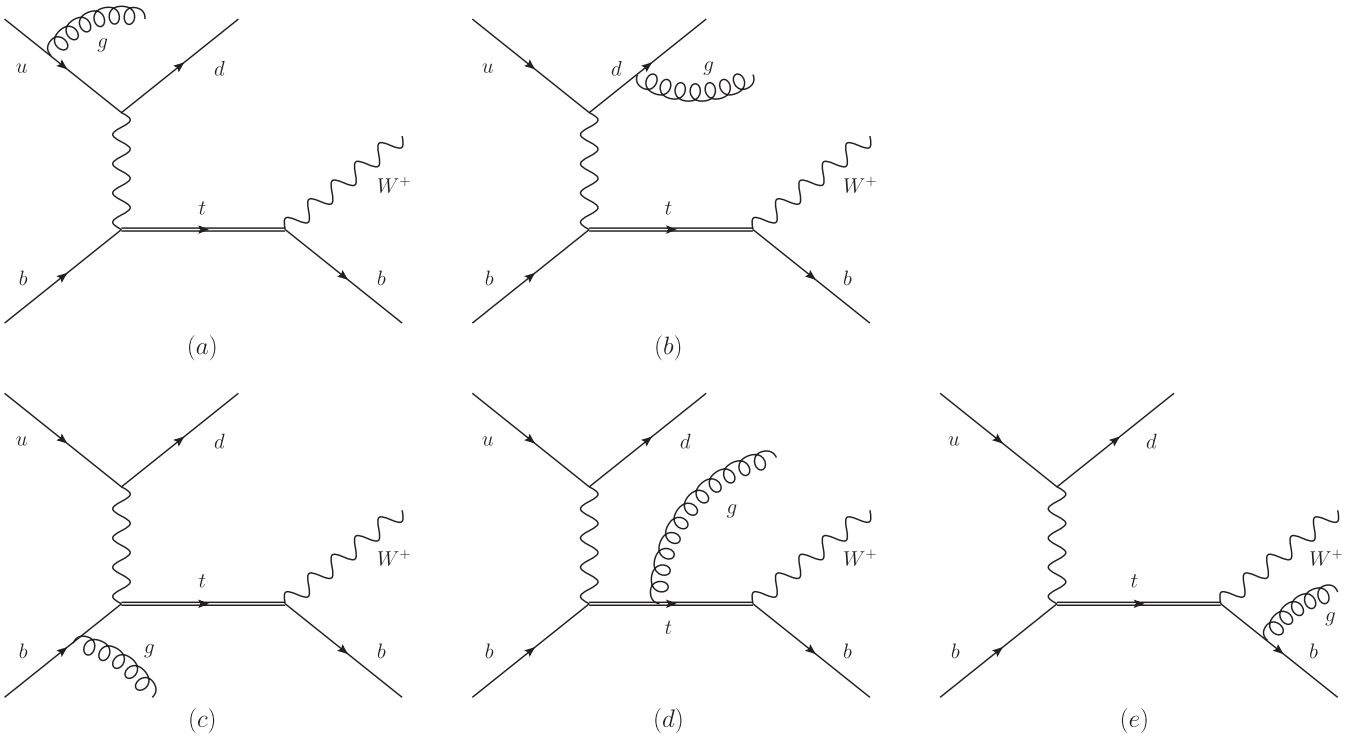

FIG. 3. Real QCD corrections to resonant t-channel single-top production at leading order in Δ_t/m_t.

$$\int d\Phi_{n+1} M_{n+1}$$
$$= \int d\Phi_{n+1}(M_{n+1} - M^{\text{sing}}_{n(+1)}) + \int d\Phi_{n+1} M^{\text{sing}}_{n(+1)}$$
$$\simeq \int d\Phi_{n+1}(M_{n+1} - M^{\text{sing}}_{n(+1)}) + \int d\Phi_{n+1} M^{\text{sing exp}}_{n(+1)}. \quad (2.15)$$

The explicit infrared poles in $M^{\text{sing exp}}_{n(+1)}$ now match the infrared poles of the virtual corrections. The error introduced in the second line of Eq. (2.15) is suppressed by a factor $\alpha_s \delta$ relative to the Born term and, therefore, is beyond the accuracy we are aiming at. It corresponds to the error introduced in expanding the virtual corrections. Treating the real corrections in this way, we ensure that the expansion of the real and virtual corrections in Δ_t/m_t is performed in a consistent way, such that the infrared poles always match. We have implemented this procedure in two independent programs, using the FKS [47] and dipole subtraction [48] methods. The agreement of the results produced with the two programs provides us with a useful check of the implementation.

III. HELICITY AMPLITUDES FOR SINGLE-TOP PRODUCTION

In this section we present all the helicity amplitudes necessary for the computation of the $\mathcal{O}(\delta)$ and $\mathcal{O}(\delta^{3/2})$ contributions to the cross section of the process (2.1). These consist of the leading resonant tree-level diagram [1(a)] shown in Fig. 1, which scales as $\delta^{1/2}$, and of virtual and real QCD corrections to this diagram ([including the gluon-initiated processes Eqs. (2.14) and (2.13)], which scale parametrically as $\delta^{1/2}\alpha_s \sim \delta$. The resummation of finite-width effects, illustrated in Eq. (2.5), also requires the calculation of one-loop electroweak self-energies, as discussed in Secs. III B and III C. Any other contribution is suppressed by at least δ compared to the leading tree-level process and is beyond the accuracy pursued in this work. The inclusion of real corrections in our formalism has been discussed in the previous section, and here we limit ourselves to giving a list of the relevant amplitudes. For the virtual corrections we will explain, in some detail, the application of the method of regions to the computation of the expansion in δ of loop integrals. Throughout this section, and the rest of the paper, we adopt the helicity notation introduced in Ref. [49,50] and make use of the following abbreviations: $s_{ij} \equiv (p_i + p_j)^2$, $p_t \equiv p_4 + p_5 + p_6$, $D_t \equiv p_t^2 - m_t^2$, and $\Delta_t \equiv p_t^2 - \mu_t^2$.

A. Tree-level amplitude

As pointed out in Sec. II A, of the tree-level diagrams shown in Fig. 1 only the resonant one, diagram 1(a), contributes to the amplitude at $\mathcal{O}(\delta^{1/2})$. Given its purely electroweak nature, the only nonvanishing amplitude is the one for the helicity configuration $u_L b_L \to d_L b_L e_R^+ \nu_L$ and it reads

$$g_{\text{ew}}^3 A^{(3,0)}_{(-1)} = g_{\text{ew}}^4 \sqrt{\frac{\pi}{M_W \Gamma_W}} \frac{[12]\langle 46\rangle\langle 3|4+6|5]}{(s_{13} + M_W^2)\Delta_t}. \quad (3.1)$$

In Eq. (3.1), the extra power of the coupling constant, g_{ew}, and the prefactor $\sqrt{\pi/M_W\Gamma_W}$ arise from the inclusion of the W-boson decay in the improved narrow-width approximation; $1/((p_W^2 - M_W^2)^2 + M_W^2\Gamma_W^2) \sim \pi/(M_W\Gamma_W)\delta(p_W^2 - M_W^2)$. Note, however, that this prefactor does not modify the scaling of the amplitude since $\Gamma_W \propto g_{\text{ew}}^2$. The complex pole, $\mu_t^2 \equiv m_t^2 - i m_t \Gamma_t$, in the top-quark propagator, Δ_t, resums leading finite-width effects and can be related order-by-order in α_s, α_{ew} to the renormalized mass and self-energy of the top quark. This is explicitly shown below in Sec. III C. The amplitude $A^{(3,0)}_{(-1)}$ is formally gauge independent, up to terms suppressed by δ or higher. These gauge-violating terms, which would normally be cancelled by the electroweak background diagrams in Fig. 1, are numerically small as long as the condition $\delta \ll 1$ is satisfied. For the input parameters and cuts adopted in Sec. IV, they amount to a correction to the leading resonant contribution to the cross section of much less than 1%. However, when $\delta \gtrsim 1$ the effective-theory expansion breaks down and these parametrically suppressed contributions can be numerically important. In this case it is necessary to calculate the complete gauge-invariant set of diagrams, shown in Fig. 1.

B. Virtual corrections

The relevant one-loop contributions to the amplitude up to $\mathcal{O}(\delta)$ are shown in Fig. 2. As mentioned in Sec. II B, we use the method of regions [35] to compute these loop integrals. This automatically yields the expansion of the full integral in δ and has the advantage of simplifying the calculation. In the case of interest here, the two relevant momentum regions are *soft* ($q_0 \sim \vec{q} \sim \delta$) and *hard* ($q_0 \sim \vec{q} \sim 1$). Only the hard part of the electroweak self-energy diagram [2(b)] contributes to the amplitude at order δ, and this is automatically included in the cross section through the resummation of finite-width effects in the top-quark propagator, as explained in Sec. III C. Therefore, we focus here on the remaining QCD diagrams, 2(a) and 2(c)–2(f).

To illustrate how the expansion by regions works we will now explicitly show how it is applied to the case of diagram 2(d), starting with the computation of the soft part. The full expression for the three-point loop integral is

$$A^{(3,2)}_{(-1),d} = \alpha_s C_F \int \frac{d^d q}{(2\pi)^d} \times \frac{\ldots(\not{p}_t - m_t)\gamma^\mu(\not{p}_t - \not{q} - m_t)\ldots(\not{p}_2 - \not{q})\gamma_\mu u(p_2)}{q^2(q^2 - 2p_t\cdot q + D_t)(q^2 - 2p_2\cdot q)}, \quad (3.2)$$

where the ellipses denote constants and spinor quantities which do not depend on the loop momentum, q. Let us first consider the expansion of the three propagators appearing in the denominator. The gluon propagator has an homogeneous scaling, since all the components of q are of order δ, and is not expanded. In the light-fermion propagator, $q^2 - 2p_2 \cdot q$, the quadratic term ($\sim \delta^2$) is suppressed compared to the linear term ($\sim \delta$) and can be dropped. Therefore, $q^2 - 2p_2 \cdot q \to -2p_2 \cdot q$. In the top-quark propagator, the term quadratic in q can again be neglected, whereas $p_2 \cdot q$ and D_t both scale as δ. Furthermore, given that $D_t - 2p_t \cdot q \sim \delta$ in the soft region, finite-width effects must be resummed to all orders in the top-quark propagator, leading to

$$\frac{1}{q^2 - 2p_t \cdot q + D_t} \to \frac{1}{\Delta_t - 2p_t \cdot q}. \tag{3.3}$$

In the numerator of Eq. (3.2), the loop momentum, q, is always parametrically smaller than the external momenta, p_i, and can be neglected at leading order in δ. From the properties of the Dirac algebra and of the spinors, $u(p)$, it also follows that

$$\not{p}_2 \gamma_\mu u(p_2) = 2p_{2,\mu} u(p_2), \tag{3.4}$$

$$\begin{aligned}(\not{p}_t - m_t)\gamma^\mu(\not{p}_t - m_t) &= 2p_t^\mu(\not{p}_t - m_t) - D_t\gamma^\mu \\ &\sim 2p_t^\mu(\not{p}_t - m_t),\end{aligned} \tag{3.5}$$

where we have used $D_t \sim \delta$ to drop the second term. Thus, the leading soft contribution to the loop integral (3.2) is

$$A^{(3,2)S}_{(-1),d} = \alpha_s C_F (4p_2 \cdot p_t) \int \frac{d^d q}{(2\pi)^d} \times \frac{\ldots(\not{p}_t - m_t)\ldots u(p_2)}{q^2(\Delta_t - 2p_t \cdot q)(-2p_2 \cdot q)}. \tag{3.6}$$

Note that the leading soft part in the expansion by regions is equivalent to the well-known eikonal approximation,

$$\frac{(\not{p}_2 - \not{q})\gamma^\mu}{(p_2 - q)^2} \to \frac{p_2^\mu}{(-p_2 \cdot q)}. \tag{3.7}$$

Equation (3.6) is much simpler than the original integral (3.2) and can be easily computed with standard techniques. The explicit result is given in Eq. (3.8). The parametric scaling of the correction (3.6) can actually be checked before the explicit calculation of the integral. Given that a soft momentum scales as δ; the gluon propagator scales as δ^{-2}, the light-quark and top-quark propagator as δ^{-1}, and the infinitesimal volume element d^4q as δ^4. Thus, Eq. (3.8) is suppressed compared to the leading amplitude by $\alpha_s \times \delta^4 \times \delta^{-2}\delta^{-1}\delta^{-1} \sim \delta^{1/2}$, as expected.

The remaining QCD diagrams in Fig. 2 can be expanded in the soft region analogously to diagram 2(d). As a consequence of the simple structure of the quark-gluon vertex in the soft limit, Eq. (3.7), the soft corrections factorize in terms of scalar functions and the leading tree-level amplitude, $A^{(3,0)}_{(-1)}$. The contributions of the different diagrams in Fig. 2 read as follows [$\tilde{\mu}^{2\epsilon} \equiv e^{\epsilon\gamma_E}\mu^{2\epsilon}/(4\pi)^\epsilon$ with μ being the renormalization scale]:

$$A^{(3,2)S}_{(-1),a} = \left[-16\pi i\alpha_s C_F \tilde{\mu}^{2\epsilon}\frac{m_t^2}{\Delta_t}\int\frac{d^dq}{(2\pi)^d}\frac{1}{q^2}\frac{1}{\Delta_t - 2p_t\cdot q}\right]A^{(3,0)}_{(-1)} = \frac{\alpha_s C_F}{2\pi}\left[\frac{1}{\epsilon} + 2\right]\left(-\frac{\Delta_t}{\mu m_t}\right)^{-2\epsilon}A^{(3,0)}_{(-1)},$$

$$A^{(3,2)S}_{(-1),c} = \left[-16\pi i\alpha_s C_F \tilde{\mu}^{2\epsilon}(p_1\cdot p_3)\int\frac{d^dq}{(2\pi)^d}\frac{1}{q^2}\frac{1}{(-2p_1\cdot q)}\frac{1}{(-2p_3\cdot q)}\right]A^{(3,0)}_{(-1)} = 0,$$

$$\begin{aligned}A^{(3,2)S}_{(-1),d} &= \left[-16\pi i\alpha_s C_F \tilde{\mu}^{2\epsilon}(p_2\cdot p_t)\int\frac{d^dq}{(2\pi)^d}\frac{1}{q^2}\frac{1}{(-2p_2\cdot q)}\frac{1}{\Delta_t - 2p_t\cdot q}\right]A^{(3,0)}_{(-1)} \\ &= \frac{\alpha_s C_F}{2\pi}\left[\frac{1}{2\epsilon^2} + \frac{5}{24}\pi^2\right]\left(-\frac{\Delta_t}{\mu m_t}\right)^{-2\epsilon}A^{(3,0)}_{(-1)},\end{aligned}$$

$$\begin{aligned}A^{(3,2)S}_{(-1),e} &= \left[-16\pi i\alpha_s C_F \tilde{\mu}^{2\epsilon}(p_4\cdot p_t)\int\frac{d^dq}{(2\pi)^d}\frac{1}{q^2}\frac{1}{(-2p_4\cdot q)}\frac{1}{\Delta_t - 2p_t\cdot q}\right]A^{(3,0)}_{(-1)} \\ &= \frac{\alpha_s C_F}{2\pi}\left[\frac{1}{2\epsilon^2} + \frac{5}{24}\pi^2\right]\left(-\frac{\Delta_t}{\mu m_t}\right)^{-2\epsilon}A^{(3,0)}_{(-1)},\end{aligned}$$

$$\begin{aligned}A^{(3,2)S}_{(-1),f} &= \left[-16\pi i\alpha_s C_F \tilde{\mu}^{2\epsilon}(p_2\cdot p_4)\int\frac{d^dq}{(2\pi)^d}\frac{1}{q^2}\frac{1}{(-2p_2\cdot q)}\frac{1}{(-2p_4\cdot q)}\frac{\Delta_t}{\Delta_t - 2p_t\cdot q}\right]A^{(3,0)}_{(-1)} \\ &= \frac{\alpha_s C_F}{2\pi}\left[-\frac{1}{\epsilon^2} - \frac{1}{\epsilon}\ln\left(\frac{(s_{2t} - m_t^2)(s_{4t} - m_t^2)}{m_t^2 s_{24}}\right) + \mathrm{Li}_2\left(1 - \frac{(s_{2t} - m_t^2)(s_{4t} - m_t^2)}{m_t^2 s_{24}}\right) - \frac{5}{12}\pi^2\right]\left(-\frac{\Delta_t}{\mu m_t}\right)^{-2\epsilon}A^{(3,0)}_{(-1)}.\end{aligned} \tag{3.8}$$

In the soft limit, diagram 2(c) reduces to a scaleless integral that vanishes in dimensional regularization. This is a consequence of the fact that the upper quark line of the tree-level diagram 1(a) does not carry any information about the off-shellness of the intermediate top-quark propagator, and is thus not sensitive to the soft scale, $m_t\delta$. The total soft correction is

$$A^{(3,2)S}_{(-1)} = \sum_i A^{(3,2)S}_{(-1),i} = \delta V^S A^{(3,0)}_{(-1)},$$

$$\delta V^S = \frac{\alpha_s C_F}{2\pi}\left(-\frac{\Delta_t}{\mu m_t}\right)^{-2\epsilon} \times\left[\frac{1}{\epsilon}\left(1-\ln\left(\frac{(s_{2t}-m_t^2)(s_{4t}-m_t^2)}{m_t^2 s_{24}}\right)\right)+2 + \mathrm{Li}_2\left(1-\frac{(s_{2t}-m_t^2)(s_{4t}-m_t^2)}{m_t^2 s_{24}}\right)\right]. \quad (3.9)$$

In the hard region, the loop momentum scales as $q\sim 1$ and cannot be neglected in the numerator or denominator of Eq. (3.2). In this case, however, $p_t^2 - m_t^2 \sim \delta$ is much smaller than any other invariant and one can expand the integrand of Eq. (3.2) in D_t. The leading hard contribution for diagram 2(d) then reads

$$A^{(3,2)H}_{(-1),d} = \alpha_s C_F \int \frac{d^dq}{(2\pi)^d} \times \frac{\ldots(\not p_t - m_t)\gamma^\mu(\not p_t - \not q - m_t)\ldots(\not p_2 - \not q)\gamma_\mu u(p_2)}{q^2(q^2-2p_t\cdot q)(q^2-2p_2\cdot q)}. \quad (3.10)$$

As for the soft region, the expansion in δ leads to a significant simplification of the integrand. Note that, in the hard region, there is no resummation of self-energy insertions, since by assumption $q^2 - 2p_t\cdot q \sim m_t^2$. Furthermore, at leading order in δ, the hard part of (3.2) coincides with the one-loop vertex correction to the on-shell single-top production process $u(p_1)b(p_2)\to d(p_3)t(p_t)$, with $p_t^2 = m_t^2$. In the effective-theory language this is equivalent to the statement that the hard matching coefficients are obtained from the computation of fixed-order on-shell matrix elements. Strictly speaking, in this context the term "on-shell" would imply $p_t^2 = \mu_t^2$. However, this condition must be satisfied only order-by-order in $\alpha_s^2 \sim \alpha_{\rm ew} \sim \delta$, and for an $\mathcal{O}(\delta)$ calculation we can simply set $p_t^2 = m_t^2$ in the leading hard contributions. Using the counting scheme (2.6) we can again determine the scaling behavior of Eq. (3.10), which is, in this case, $\alpha_s \times 1 \times 1 \sim \delta^{1/2}$, since all momenta scale as ~ 1. This is confirmed by the explicit result given below in Eq. (3.12).

Applying the hard-region expansion to diagrams 2(c)–2(f) we obtain

$$A^{(3,2)H}_{(-1),c} = \delta V^H_{13} A^{(3,0)}_{(-1)},$$

$$A^{(3,2)H}_{(-1),d} = \delta V^H_{2t} A^{(3,0)}_{(-1)} + \frac{g_{\rm ew}}{2}\sqrt{\frac{\pi}{M_W\Gamma_W}}\frac{[52]\langle 46\rangle\langle 3|2|1]}{(s_{13}+M_W^2)\Delta_t} \times \frac{\alpha_s C_F}{2\pi}\frac{m_t^2}{2m_t^2 - s_{2t}}\ln\left(\frac{s_{2t}-m_t^2}{m_t^2}\right),$$

$$A^{(3,2)H}_{(-1),e} = \delta V^H_{4t} A^{(3,0)}_{(-1)} + \frac{g_{\rm ew}}{2}\sqrt{\frac{\pi}{M_W\Gamma_W}}\frac{[12]\langle 43\rangle\langle 6|4|5]}{(s_{13}+M_W^2)\Delta_t} \times \frac{\alpha_s C_F}{2\pi}\frac{m_t^2}{2m_t^2 - s_{4t}}\ln\left(\frac{s_{4t}-m_t^2}{m_t^2}\right),$$

$$A^{(3,2)H}_{(-1),f} = 0, \quad (3.11)$$

where the three scalar functions δV^H_{13}, δV^H_{2t}, δV^H_{4t} are given by

$$\delta V^H_{13} = \frac{\alpha_s C_F}{2\pi}\left[-\frac{1}{\epsilon^2}+\frac{1}{\epsilon}\left(\ln\left(\frac{s_{13}}{\mu^2}\right)-\frac{3}{2}\right)-\frac{1}{2}\ln^2\left(\frac{s_{13}}{\mu^2}\right)+\frac{3}{2}\ln\left(\frac{s_{13}}{\mu^2}\right)-4+\frac{x_{\rm sc}}{2}+\frac{\pi^2}{12}\right],$$

$$\delta V^H_{2t} = \frac{\alpha_s C_F}{2\pi}\left[-\frac{1}{2\epsilon^2}+\frac{1}{\epsilon}\left(\ln\left(\frac{s_{2t}-m_t^2}{m_t\mu}\right)-\frac{1}{2}\right)+\mathrm{Li}_2\left(1-\frac{m_t^2}{s_{2t}-m_t^2}\right)-2+\frac{x_{\rm sc}}{2}-\frac{\pi^2}{24}-\frac{1}{2}\ln^2\left(\frac{s_{2t}-m_t^2}{m_t\mu}\right)+\frac{1}{8}\ln^2\left(\frac{m_t^2}{\mu^2}\right) + \frac{s_{2t}-m_t^2}{4(2m_t^2-s_{2t})}\ln\left(\frac{m_t^2}{\mu^2}\right)+\ln\left(\frac{s_{2t}-m_t^2}{m_t\mu}\right)\left(1-\frac{s_{2t}-m_t^2}{2(2m_t^2-s_{2t})}-\frac{1}{2}\ln\left(\frac{m_t^2}{\mu^2}\right)\right)\right],$$

$$\delta V^H_{4t} = \delta V^H_{2t}|_{s_{2t}\to s_{4t}}. \quad (3.12)$$

The expressions in Eq. (3.12), once renormalized as explained in the next section, agree with the results available in the literature [see, e.g,. Eq. (19) of Ref. [9] and Eq. (9) of Ref. [18]]. This is expected, since the leading hard contributions must coincide with the corresponding corrections to the on-shell top production process. The value of the parameter $x_{\rm sc}$ in Eq. (3.12) depends on the particular version of dimensional regularization used for the calculation (see, e.g., Ref. [51]), and is given by $x_{\rm sc} = 0$ in the 't Hooft-Veltman scheme and $x_{\rm sc} = 1$ in the four-dimensional helicity scheme. As anticipated in Sec. II B, the $\mathcal{O}(\alpha_s\delta^{1/2})$ hard contribution of diagram 2(f) vanishes since the intermediate top-quark propagator is off-shell by an amount $\sim m_t^2$. This leads to a further suppression in δ compared to the other one-loop QCD diagrams shown in Fig. 2. In a strict effective-theory approach, the contribution of diagram 2(f) would be encoded in an effective higher-dimensional $bW^+\to bW^+$ vertex.

The expansion of the self-energy diagram 2(a) in the hard region presents some subtleties. Let us consider the leading (fixed-order) top-quark propagator, $i(\not p_t + m_t)/D_t$, and the QCD self-energy correction to the propagator,

$$\frac{i(\not{p}_t + m_t)}{D_t}\Big[-4\pi\alpha_s C_F \tilde{\mu}^{2\epsilon}\int\frac{d^dq}{(2\pi)^d} \times \frac{\gamma^\alpha(\not{p}_t - \not{q} + m_t)\gamma_\alpha}{q^2(q^2 - 2p_t\cdot q + D_t)}\Big]\frac{i(\not{p}_t + m_t)}{D_t}. \tag{3.13}$$

By applying our counting to Eq. (3.13), one expects the leading hard contribution of the QCD self-energy correction to scale as $\alpha_s\delta^{-2} \sim \delta^{-3/2}$, i.e., it is enhanced by $\delta^{-1/2}$ with respect to the leading-order propagator, which scales as δ^{-1}. Hence, in this case we have to push the expansion by regions one order further to include all the terms suppressed by $\delta^{1/2}$ compared to the leading tree-level contribution. Thus, the expansion of Eq. (3.13) in D_t, up to the relevant order, is

$$\frac{\alpha_s C_F}{2\pi}\Big[\frac{3}{2\epsilon} + 2 + \frac{x_{\rm sc}}{2}\Big]\Big(\frac{m_t^2}{\mu^2}\Big)^{-\epsilon}\Big[\frac{2im_t^2(\not{p}_t + m_t)}{D_t^2} + \frac{im_t}{D_t} - \frac{i(\not{p}_t + m_t)}{D_t}\Big]. \tag{3.14}$$

As anticipated, the first term in Eq. (3.14) is "superleading" and in a generic renormalization scheme has to be resummed in the top-quark propagator. However, in the on-shell scheme adopted in this paper, the superleading bit is cancelled exactly by the top-quark mass counterterm, as shown in Sec. III C.

As pointed out at the beginning of this section, only the hard part of the electroweak self-energy diagram 2(b) is relevant to our calculation since a soft contribution would scale as $\delta^{1/2}\alpha_{\rm ew} \sim \delta^{3/2}$. In this case, the dominant hard correction to the propagator scales as $\alpha_{\rm ew}\delta^{-2} \sim \delta^{-1}$ and is resummed, while higher-order terms are beyond the target accuracy pursued here and can be neglected. In principle, diagrams analogous to 2(b), but with a photon or a Z boson in the loop, should also be resummed. As we will see in the next section, in the on-shell scheme only the imaginary part of the one-loop two-point function is effectively resummed in the propagator, and diagram 2(b) is therefore sufficient.

C. Renormalization and resummation of finite-width effects

We now discuss the renormalization of the one-loop amplitudes computed in Sec. III B. In this paper we adopt the on-shell scheme (see, e.g., Refs. [52,53]). In this scheme, the wave-function counterterms for external massless particles vanish identically, i.e., $\delta Z_i = 0$ for $i = 1, \ldots, 6$. Furthermore, the electroweak coupling, $g_{\rm ew}$, is not renormalized at $\mathcal{O}(\alpha_s)$. Thus, the only counterterm relevant for our calculation is the top-quark mass counterterm, δm_t. This induces a renormalization of the top-quark propagator, which is

$$\frac{i(\not{p}_t + m_t)}{D_t}(-i\delta m_t)\frac{i(\not{p}_t + m_t)}{D_t} = \frac{\delta m_t}{m_t}\Big[\frac{2im_t^2(\not{p}_t + m_t)}{D_t^2} + \frac{im_t}{D_t}\Big], \tag{3.15}$$

with the $\mathcal{O}(\alpha_s)$ mass counterterm given by

$$\frac{\delta m_t}{m_t} = -\frac{\alpha_s C_F}{2\pi}\Big[\frac{3}{2\epsilon} + 2 + \frac{x_{\rm sc}}{2}\Big]\Big(\frac{m_t^2}{\mu^2}\Big)^{-\epsilon}. \tag{3.16}$$

Comparing Eqs. (3.14) and (3.15), it is clear that the superleading terms (and part of the subleading ones) arising from the self-energy correction are cancelled by the counterterm. Rewriting Eqs. (3.14) and (3.15) as contributions to the amplitude, one obtains

$$A^{(3,2)H}_{(-1),a} + A^{(3,2),\rm ren}_{(-1)} = \frac{\alpha_s C_F}{2\pi}\Big[-\frac{3}{2\epsilon} - 2 - \frac{x_{\rm sc}}{2}\Big] \times \Big(\frac{m_t^2}{\mu^2}\Big)^{-\epsilon} A^{(3,0)}_{(-1)}. \tag{3.17}$$

In an arbitrary renormalization scheme, which in the following we will denote by r, there is, in general, no exact cancellation of the superleading contributions in Eqs. (3.14) and (3.15), and these terms are resummed inside the complex pole of the top-quark propagator, $\mu_t^2 \equiv m_t^2 - im_t\Gamma_t$. Consider the renormalized top-quark two-point function,

$$\bar{\Gamma}_t(\not{p}) \equiv \not{p} - m_{t,r} + \bar{\Sigma}_{t,r}(\not{p}), \tag{3.18}$$

where $m_{t,r}$ is the renormalized mass in the generic scheme r and $\bar{\Sigma}_{t,r}$ represents the renormalized top-quark self-energy. The complex pole, μ_t, is defined as the solution for $\not{p}$ at which Eq. (3.21) vanishes (see, e.g., Ref. [54]). Since $\Delta_t \sim \delta$, Eq. (3.18) must include all contributions to $\bar{\Sigma}_{t,r}$ up to $\mathcal{O}(\delta)$, i.e., the one-loop QCD ($\sim\alpha_s \sim \delta^{1/2}$) and electroweak ($\sim\alpha_{\rm ew} \sim \delta$) top-quark self-energies, and the two-loop QCD contribution ($\sim\alpha_s^2 \sim \delta$). Other corrections to $\bar{\Sigma}_{t,r}$ can be included perturbatively and need not to be resummed.

In the following we will adopt the notation of Ref. [53] and parametrize the top-quark self-energy as

$$\bar{\Sigma}_{t,r}(\not{p}) = \bar{\Sigma}^L_{t,r}(p^2)\not{p}P_L + \bar{\Sigma}^R_{t,r}(p^2)\not{p}P_R + \bar{\Sigma}^S_{t,r}(p^2)m_{t,r}. \tag{3.19}$$

The renormalized quantities in Eq. (3.19) are related to the unrenormalized ones by

$$\begin{aligned}\bar{\Sigma}^L_{t,r}(p^2) &= \Sigma^L_t(p^2) + \delta Z^L_{t,r},\\ \bar{\Sigma}^R_{t,r}(p^2) &= \Sigma^R_t(p^2) + \delta Z^R_{t,r},\\ \bar{\Sigma}^S_{t,r}(p^2) &= \Sigma^S_t(p^2) - \frac{\delta m_{t,r}}{m_{t,r}} - \frac{\delta Z^L_{t,r} + \delta Z^R_{t,r}}{2},\end{aligned} \tag{3.20}$$

where $\delta m_{t,r}$ and $\delta Z_{t,r}^{L/R}$ denote the mass and wave-function counterterms, in the scheme r, respectively. Equation (3.18) can be rewritten in a form more suitable to the extraction of the pole by inserting identity matrices, in the form $\mathbf{I} = (\not{p} - m_{t,r})(\not{p} + m_{t,r})/(p^2 - m_{t,r}^2)$, at both sides of $\bar{\Sigma}_{t,r}$ and expanding the quantity $(\not{p} + m_{t,r})\bar{\Sigma}_{t,r}(\not{p} + m_{t,r})$ around $p^2 = m_{t,r}^2$. This leads to

$$\begin{aligned}\bar{\Gamma}_t(\not{p}) &= \not{p} - m_{t,r} + m_{t,r}^2\bar{\Omega}_{t,r}(p^2)\frac{\not{p} - m_{t,r}}{p^2 - m_{t,r}^2} \\ &\quad + m_{t,r}^2[2\bar{\Sigma}_{t,r}^L(p^2) + 2\bar{\Sigma}_{t,r}^R(p^2) + \bar{\Omega}_{t,r}(p^2)] \\ &\quad \times \frac{(\not{p} - m_{t,r})^3}{(p^2 - m_{t,r}^2)^2} + \ldots, \end{aligned} \tag{3.21}$$

where the ellipsis indicates terms that are suppressed beyond $\mathcal{O}(\delta)$ and, thus, are irrelevant to the calculation presented here. For later convenience, in Eq. (3.21) we have introduced the function $\bar{\Omega}_{t,r} = \bar{\Sigma}_{t,r}^L + \bar{\Sigma}_{t,r}^R + 2\bar{\Sigma}_{t,r}^S$.

The complex mass, μ_t, is obtained by solving the equation $\bar{\Gamma}_t(\mu_t) = 0$, and reads

$$\begin{aligned}\mu_t &= m_{t,r} - \frac{m_{t,r}}{2}\bar{\Omega}_{t,r}(m_{t,r}^2) + \frac{m_{t,r}}{4}\bar{\Omega}_{t,r}(m_{t,r}^2) \\ &\quad \times \left[\bar{\Sigma}_{t,r}^L(m_{t,r}^2) + \bar{\Sigma}_{t,r}^R(m_{t,r}^2) + 2m_{t,r}^2\frac{\partial\bar{\Omega}_{t,r}}{\partial p^2}(m_{t,r}^2)\right]. \end{aligned} \tag{3.22}$$

Equation (3.22) can be further expanded in α_s and $\alpha_{\rm ew}$. To this end, we introduce a decomposition of the self-energies analogous to Eq. (2.7)

$$\begin{aligned}\bar{\Sigma}_{t,r}^S &= \alpha_s\bar{\Sigma}_{t,r}^{S,(0,2)} + \alpha_s^2\bar{\Sigma}_{t,r}^{S,(0,4)} + \alpha_{\rm ew}\bar{\Sigma}_{t,r}^{S,(2,0)}, \\ \bar{\Sigma}_{t,r}^{L/R} &= \alpha_s\bar{\Sigma}_{t,r}^{V,(0,2)} + \alpha_s^2\bar{\Sigma}_{t,r}^{V,(0,4)} + \alpha_{\rm ew}\bar{\Sigma}_{t,r}^{L/R,(2,0)}. \end{aligned} \tag{3.23}$$

Note that the pure QCD part of the self-energy does not have an axial component, and $\bar{\Sigma}_{t,r}^{L,(0,n)} = \bar{\Sigma}_{t,r}^{R,(0,n)} \equiv \bar{\Sigma}_{t,r}^{V,(0,n)}$ for $n = 2, 4$. Using Eqs. (3.22) and (3.23) one can easily obtain the following results for the pole mass and width:

$$\begin{aligned}m_t &\equiv \mathrm{Re}[\mu_t] \\ &= m_{t,r} - \alpha_s m_{t,r}(\bar{\Sigma}_{t,r}^{V,(0,2)} + \bar{\Sigma}_{t,r}^{S,(0,2)}) - \alpha_s^2 m_{t,r}(\bar{\Sigma}_{t,r}^{V,(0,4)} \\ &\quad + \bar{\Sigma}_{t,r}^{S,(0,4)}) + \alpha_s^2 m_{t,r}(\bar{\Sigma}_{t,r}^{V,(0,2)} + \bar{\Sigma}_{t,r}^{S,(0,2)}) \\ &\quad \times \left[\bar{\Sigma}_{t,r}^{V,(0,2)} + 2m_{t,r}^2\left(\frac{\partial\bar{\Sigma}_{t,r}^{V,(0,2)}}{\partial p^2} + \frac{\partial\bar{\Sigma}_{t,r}^{S,(0,2)}}{\partial p^2}\right)\right] \\ &\quad - \alpha_{\rm ew}\frac{m_{t,r}}{2}\left(\mathrm{Re}[\bar{\Sigma}_{t,r}^{L,(2,0)}] + \bar{\Sigma}_{t,r} + 2\bar{\Sigma}_{t,r}^{S,(2,0)}\right), \\ \Gamma_t &\equiv -2\,\mathrm{Im}[\mu_t] = \alpha_{\rm ew}m_{t,r}\,\mathrm{Im}[\bar{\Sigma}_{t,r}^{L,(2,0)}], \end{aligned} \tag{3.24}$$

where we have used the information that only $\bar{\Sigma}_{t,r}^{L,(2,0)}$ has a nonvanishing imaginary part, and all the functions are evaluated at $p^2 = m_{t,r}^2$.

In the on-shell scheme (os), Eq. (3.24) assumes a particularly simple structure:

$$m_t = m_{t,\rm os}, \qquad \Gamma_t = \alpha_{\rm ew}m_{t,\rm os}\,\mathrm{Im}[\Sigma_t^{L,(2,0)}(m_{t,\rm os}^2)]. \tag{3.25}$$

The result (3.25) follows from the particular form of the mass and field counterterms in this scheme [53]:

$$\begin{aligned}\delta m_{t,\rm os} &= \frac{m_{t,\rm os}}{2}\,\mathrm{Re}[\Sigma_t^L + \Sigma_t^R + 2\Sigma_t^S], \\ \delta Z_{t,\rm os}^{L,R} &= -\mathrm{Re}\left[\Sigma_t^{L/R} + m_{t,\rm os}^2\left(\frac{\partial\Sigma_t^L}{\partial p^2} + \frac{\partial\Sigma_t^R}{\partial p^2} + 2\frac{\partial\Sigma_t^S}{\partial p^2}\right)\right]. \end{aligned} \tag{3.26}$$

Thus, at the level of accuracy we are interested in, the pole mass, m_t, can be identified with the on-shell mass, $m_{t,\rm os}$.[3] Furthermore, as anticipated at the end of Sec. III B, only the imaginary part of the one-loop electroweak self-energy is effectively resummed in the propagator. In particular, in Eq. (3.25) the dependence from the one-loop (and two-loop) QCD contributions, which are responsible for the superleading terms in Eqs. (3.14) and (3.15), cancels completely. The imaginary part of the complex pole is given, as expected, by the on-shell top decay width

$$\Gamma_t = \frac{G_F}{8\pi\sqrt{2}}m_t^3\left(1 - \frac{M_W^2}{m_t^2}\right)^2\left(1 + 2\frac{M_W^2}{m_t^2}\right). \tag{3.27}$$

The residue of the propagator at the complex pole, δR_t, which enters Eq. (2.5), can be easily extracted from Eq. (3.21) and expanded in α_s and $\alpha_{\rm ew}$ up to the required accuracy. Here we only mention the fact that in a generic scheme $\delta R_{t,r} \sim \alpha_s + \ldots$, and the term $\delta R_{t,r}A_{(-1)}^{(3,0)}$ is parametrically of the same order as the one-loop QCD corrections computed in Sec. III B. Thus, it also contributes to the amplitude at order δ. However, in the on-shell scheme, the expansion of $\delta R_{t,\rm os}$ starts at order $\alpha_{\rm ew}$ and contributes a correction to the amplitude which is beyond the accuracy pursued here.

We would like to conclude this section with a remark on how a ''bad'' choice of renormalization scheme can lead to a breakdown of the effective-theory counting scheme, Eq. (2.6). Throughout this paper we assumed the scalings $D_t \equiv p_t^2 - m_{t,r}^2 \sim \delta$ and $\Delta_t \equiv p_t^2 - \mu_t^2 \sim \delta$ for the bare and resummed top-quark propagator. This is consistent in the on-shell scheme as $\mu_t^2 - m_{t,\rm os}^2 = \mu_t^2 - m_t^2 \sim \delta$. However, in a generic renormalization scheme the two conditions are incompatible since $\mu_t^2 - m_{t,r}^2 \sim \alpha_s \sim \sqrt{\delta}$. This is a problem well known in the context of applying effective-theory methods to quarkonium physics. Thus, while in principle one could choose an arbitrary renormalization scheme (e.g., $\overline{\rm MS}$), in practice this can lead to complications and loss of transparency in the expansion in δ. In other words, the effective-theory approach adopted here naturally identifies a class of ''good'' renormalization schemes defined by the condition $m_{t,r} - m_t \sim \delta$, of which the on-shell scheme represents a particular example.

[3]It is well known that the relation (3.25) is corrected by terms of order $\alpha_{\rm ew}^2$, which are, however, beyond the accuracy pursued here.

D. Real corrections

The last class of $\mathcal{O}(\delta^{1/2}\alpha_s)$ contributions to the amplitude we have to consider are represented by real gluonic corrections to the tree-level process (2.1), i.e., $u(p_1)b(p_2) \to d(p_3)b(p_4)l^+(p_5)\nu_l(p_6)g(p_7)$. The relevant Feynman diagrams are shown in Fig. 3. The (leading) real-emission amplitude can be written as

$$\mathcal{A}^{\text{real}}_{(-1)}(g_7^{\pm}) = \delta_{24}T^{a_7}_{31}g_{\text{ew}}^3 g_s A^{(3,1)}_{[31]}(g_7^{\pm}) + \delta_{13}T^{a_7}_{42}g_{\text{ew}}^3 g_s A^{(3,1)}_{[42]}(g_7^{\pm}), \tag{3.28}$$

where $g_7^{\pm}$ denotes the two possible helicity states of the emitted gluon, and $A^{(3,1)}_{[31]}$ and $A^{(3,1)}_{[42]}$ represent the contribution of diagrams with a gluon attached to the upper or lower fermion line, respectively. The helicity amplitudes for the upperline emission read

$$A^{(3,1)}_{[31]}(g_7^+) = g_{\text{ew}}\sqrt{\frac{\pi}{M_W\Gamma_W}}\frac{\sqrt{2}\langle 46\rangle\langle 3|(4+6)|5]\langle 3|(7-1)|2]}{(s_{137}+M_W^2)\Delta_t\langle 17\rangle\langle 37\rangle},$$
$$A^{(3,1)}_{[31]}(g_7^-) = -g_{\text{ew}}\sqrt{\frac{\pi}{M_W\Gamma_W}}\frac{\sqrt{2}\langle 46\rangle[12][1|(3+7)|(4+6)|5]}{(s_{137}+M_W^2)\Delta_t[17][37]}, \tag{3.29}$$

where $s_{137} = s_{13} + s_{17} - s_{37}$. For the lower-line emission we obtain

$$A^{(3,1)}_{[42]}(g_7^+) = -g_{\text{ew}}\sqrt{\frac{\pi}{M_W\Gamma_W}}\frac{\sqrt{2}\langle 46\rangle}{(s_{13}+M_W^2)\Delta_t} \times \left(\frac{\langle 3|(4+6)|5]\langle 4|(7-2)|1]}{\langle 27\rangle\langle 47\rangle} + \frac{[12]}{\langle 47\rangle} \times \frac{\langle 3|(1+2)|7]\langle 4|6|5] - \mu_t^2\langle 34\rangle[57]}{\Delta_{t7}}\right),$$
$$A^{(3,1)}_{[42]}(g_7^-) = -g_{\text{ew}}\sqrt{\frac{\pi}{M_W\Gamma_W}}\frac{\sqrt{2}[12]}{(s_{13}+M_W^2)\Delta_{t7}} \times \left(\frac{\langle 3|(1+2)|5]\langle 6|(4+7)|2]}{[27][47]} - \frac{\langle 46\rangle}{[27]} \times \frac{\langle 3|1|2]\langle 7|(4+6)|5] + \mu_t^2\langle 37\rangle[25]}{\Delta_t}\right), \tag{3.30}$$

with $\Delta_{t7} = (p_t + p_7)^2 - \mu_t^2$. The complex mass, μ_t, in the numerator of Eq. (3.30), which follows from the on-shell matching condition, $p_t^2 = \mu_t^2$, guarantees that QCD Ward identities are satisfied exactly. As already pointed out for the hard virtual corrections computed in Sec. III B, the matching condition needs to be satisfied only order-by-order in δ, and one could equally well replace μ_t with m_t in the numerator of Eq. (3.30). This would lead to a gauge-invariance violation proportional to $\Gamma_t/m_t \sim \delta$, which is a higher-order effect in our counting scheme.

Besides the process $ub \to dbl^+\nu_l g$, at order $\delta^{1/2}\alpha_s$ the gluon-initiated processes $ug \to dbl^+\nu_l\bar{b}$ and $gb \to dbl^+\nu_l\bar{u}$ also contribute to the amplitude for single-top production. The corresponding helicity amplitudes can easily be obtained from the crossing of Eqs. (3.29) and (3.30).

E. Comparison of various approximations

The results presented in this section have been obtained by making kinematic approximations to the virtual and real corrections. Because real and virtual corrections are infrared divergent, we have to make sure that the approximations are consistent in that the real and virtual soft and collinear singularities still cancel. Since, in Sec. IV, we will be comparing our results to previous calculations, it is instructive to discuss the cancellation of infrared singularities and the relation between successive approximations to t-channel single-top production.

The first approximation we consider is to treat the top as a stable particle [7–10,26]. We will call this the stable-top calculation and denote the process by $ub \to dt$. Within this approximation, the renormalized virtual corrections read

$$A^{\text{virt}}_{ub\to dt} = A^{\text{tree}}_{ub\to dt}\left(\delta V_{13}^H + \delta V_{2t}^H + \frac{\delta m_t}{2m_t}\right) + \text{finite}, \tag{3.31}$$

where $A^{\text{tree}}_{ub\to dt}$ is the corresponding tree-level amplitude; δV_{13}^H, δV_{2t}^H, and $\delta m_t/m_t$ are given in Eqs. (3.12) and (3.16), and "finite" represents nonsingular terms that cannot be factorized in terms of the leading-order amplitude. Thus, the virtual corrections in Eq. (3.31) are precisely the leading hard corrections of diagrams 2(c) and 2(d) in Fig. 2 without the top decay, plus the renormalization of the external top-quark line, $\delta Z_t/2 = \delta m_t/(2m_t)$. The corresponding infrared singularities are cancelled, in the usual way, by the real corrections due to the process $ub \to dtg$.

The next approximation we consider is the calculation presented in Ref. [18], which we call the on-shell calculation and denote by $ub \xrightarrow{t} dbW$. In this computation, the production of an on-shell top quark is combined with the decay of an on-shell top. This leads to additional singularities in the virtual matrix element, which is given by

$$A^{\text{virt}}_{ub\xrightarrow{t}dbW} = A^{\text{tree}}_{ub\xrightarrow{t}dbW}\left(\delta V_{13}^H + \delta V_{2t}^H + \delta V_{4t}^H + \frac{\delta m_t}{m_t}\right) + \text{finite}. \tag{3.32}$$

The additional contribution, δV_{4t}^H [given in Eq. (3.12)], corresponds to the one-loop correction to the top decay, while $\delta m_t/m_t = 2 \times \delta m_t/(2m_t)$ accounts for the renormalization of the top-quark legs in the production *and* decay vertices. In order to match this with the real corrections, the latter have to be treated with some care. In particular, the interference between real gluon radiation from the production part of the process with the decay part has to be neglected. However, real corrections restricted to

either the production or decay part are taken into account and the corresponding singularities cancel those of the virtual corrections, Eq. (3.32).

In the calculation presented in this paper we move from on-shell top production to resonant-top production, indicated by a star, $ub \xrightarrow{t^*} dbW$. As discussed in the previous section, this involves a whole tower of additional contributions. However, to the accuracy we are aiming for, the only additional contribution is due to the (leading) soft part of the diagrams in Fig. 2, given in Eq. (3.8). Thus, we have additional virtual singularities, given in Eq. (3.9), and we obtain

$$A^{\text{virt}}_{ub \xrightarrow{t^*} dbW} = A^{\text{tree}}_{ub \xrightarrow{t^*} dbW}\left(\delta V^H_{13} + \delta V^H_{2t} + \delta V^H_{4t} + \frac{\delta m_t}{m_t} + \delta V^S\right) + \text{finite}, \tag{3.33}$$

with $A^{\text{tree}} = A^{(3,0)}_{(-1)}$. The new contribution, δV^S, exactly cancels the single poles in Eq. (3.32) due to soft emission off a massive top-quark leg. Thus, Eq. (3.33) contains only singularities corresponding to collinear or soft emission off massless legs, as it should for a process with only massless external states. The additional poles in δV^S are to be cancelled by real singularities which essentially correspond to those neglected in the process $ub \xrightarrow{t} dbW$, i.e., the interference between real radiation from the production and decay of the top. From a more formal point of view, one has to compute the real matrix element squared of the process $ub \to dbWg$ and expand it in δ. Because we only need the leading term in δ, it is sufficient to consider the diagrams of Fig. 3. Taking the amplitude squared corresponding to these diagrams, integrating over the phase space and expanding the result in δ leads to real singularities that precisely cancel those of the virtual corrections to the process $ub \xrightarrow{t^*} dbW$.

We stress once more that the calculation presented here is only meaningful if the top is nearly on-shell. If we are interested in the process $ub \to dbW$ with no constraint on the invariant mass of the final state particles, we have to compute the full virtual and real corrections, i.e., also take into account the diagrams that have been omitted in Figs. 2 and 3. Needless to say, such a computation is considerably more involved, but the cancellation of real and virtual singularities works in a straightforward way.

IV. RESULTS

The results for the three approximations outlined in the previous section, $ub \to dt$, $ub \xrightarrow{t} dbW$, and $ub \xrightarrow{t^*} dbW$ have been implemented using Monte Carlo integration, allowing us to calculate numerical values for both cross sections and kinematical distributions. In this section we present a selection of these results and include comparisons to existing results where available. For simplicity, throughout this section the cross sections calculated using the three approximations will be referred to as σ^{prod}, σ^t, and σ^{t^*} for the stable-top production, on-shell production followed by decay, and resonant-top calculations, respectively.

A. Total cross sections

We begin by presenting a comparison of our results, obtained using the three approximations, to those for the production of a single, stable-top quark as presented in Ref. [26]. We compare the results for an LHC run at a center of mass energy $\sqrt{s} = 10$ TeV, and use MSTW2008 PDFs [55] and the corresponding strong coupling. Renormalization and factorization scales are set to be equal to a value of $m_t/2$. The other input parameters used for this calculation are shown in Table I. In the top-quark propagator, we use the tree-level decay width for the LO cross section and the α_s-corrected width for the NLO calculation. This ensures that, at leading order, we obtain agreement between the stable-top production cross section and that of on-shell production plus decay, after integration over the fully inclusive decay of the top quark and W boson, (i.e., $\sigma_0^{\text{decay}} = \Gamma_t^{\text{LO}}$). The results of our calculations using these parameters are shown in Table II. We include the results for on-shell production taken from Table 5 of Ref. [26] for ease of comparison.

The agreement with the existing results at both leading and next-to-leading order is very good when we perform the calculation for the production of a stable top. When we also include the subsequent decay of the on-shell top we still have good agreement at LO, but we no longer agree at NLO. This discrepancy is due to the use of the improved narrow width approximation for the on-shell top. We can see from

$$\sigma_0^t = \frac{\sigma_0^{\text{prod}}\sigma_0^{\text{decay}}}{\Gamma_t^{\text{LO}}} = \frac{\sigma_0^{\text{prod}}\Gamma_t^{\text{LO}}}{\Gamma_t^{\text{LO}}} = \sigma_0^{\text{prod}} \tag{4.1}$$

that at LO the dependence on the decay width of the top quark cancels. However, at NLO there is no full cancellation and we are left with a residual dependence on the width,

TABLE I. Input parameters used for calculating the cross sections shown in Table II.

$m_t = 172$ GeV	$\Gamma_W = 2.05141$ GeV
$M_W = 80.4$ GeV	$\Gamma_t^{\text{LO}} = 1.46893$ GeV
$\alpha_{\text{ew}} = 0.03402$	$\Gamma_t^{\text{NLO}} = 1.32464$ GeV

TABLE II. Comparison of total cross sections, calculated using our three methods, to those of Campbell *et al.* [26] at leading order and next-to-leading order.

	Ref. [26]	σ^{prod}	σ^t	σ^{t^*}
LO (pb)	76.6	76.62(1)	76.62(1)	77.36(5)
NLO (pb)	84.4	84.41(1)	84.91(2)	86.3(3)

TABLE III. Comparison of total cross sections, calculated using our three methods, to those of Campbell *et al.* [18] at leading order (σ_0) and next-to-leading order (σ).

	$\sigma_0^{\rm prod} B_{t\to be\nu}$	$\sigma^{\rm prod} B_{t\to be\nu}$	σ_0^t	σ^t	$\sigma_0^{t^*}$	σ^{t^*}
Ref. [18] (pb)	17.69(1)	17.05(2)	17.69(1)	16.98(2)	N/A	N/A
Our results (pb)	17.71(1)	17.04(1)	17.71(1)	16.98(1)	17.94(1)	17.33(8)

$$\sigma^t = \frac{\sigma_0^{\rm prod}\Gamma_t^{\rm NLO} + \sigma_1^{\rm prod}\Gamma_t^{\rm LO}}{\Gamma_t^{\rm NLO}} = \sigma^{\rm prod} + \sigma_1^{\rm prod}\frac{\Gamma_t^{\rm LO} - \Gamma_t^{\rm NLO}}{\Gamma_t^{\rm NLO}}. \quad (4.2)$$

The difference between σ^t and $\sigma^{\rm prod}$ is formally a higher-order correction, since $\sigma_1^{\rm prod}(\Gamma_t^{\rm LO} - \Gamma_t^{\rm NLO}) \sim \alpha_s^2$, but leads to a visible numerical effect. From the resonant-top calculation (last column in Table II), it is clear that taking into account the nonfactorizable corrections causes a small, but noticeable increase of the cross section at both LO and NLO.

We now move on to discuss the comparison of our results to those in Ref. [18] for the on-shell production of a single-top-quark followed by its decay. We compare the results for an LHC run with center of mass energy $\sqrt{s} = 14$ TeV. The input parameters can be found in Table IV of Ref. [18]. For this comparison we set the renormalization and factorization scales equal to m_t and use the MRST2002 NLO PDFs [56] and the corresponding α_s value. The results are shown in Table III. The total cross section in the stable-top production case is obtained by multiplying the production cross section, $\sigma^{\rm prod}$, by the leading-order branching ratio for the top-quark decay, $B_{t\to be\nu} = 0.1104$.

As in the first comparison, we obtain good agreement between our results and the existing results for the stable-top production and on-shell production plus decay calculations. The inclusion of the nonfactorizable corrections again has the effect of increasing the cross sections by a modest amount at both LO and NLO.

Finally, we look at the total cross section for our minimal realistic setup, described in Sec. II A. For illustration, jets are constructed using a standard $k_\perp$ cluster algorithm with the resolution parameter set to $D_{\rm res} = 0.7$, but any other jet definition could also be used. We assume that we can always identify J_b, the jet containing the b quark. We apply cuts on $p_T(J_b)$ and $p_T(e)$, the transverse momenta of J_b and the positron, respectively, and on the transverse missing energy, $\not{E}_T$. In addition, we require that the invariant top mass, which is defined as

$$m_{\rm inv} = \sqrt{(p(J_b) + p(e) + p(\nu))^2}, \quad (4.3)$$

be close to the top-quark resonance. We perform the calculation for an LHC run with $\sqrt{s} = 7$ TeV and use the MSTW2008 NLO PDFs. The renormalization and factorization scales are set to $m_t/2$. A full list of the input parameters and cuts can be found in Table IV. We use NLO PDFs and the NLO top decay width at all times to accentuate the off-shell effects by ensuring that the corrections are not coming from the change of PDF or width. As we now apply cuts to the decay products of the top quark, it is no longer possible to include the stable-top production calculation, as this requires fully inclusive decays.

The results for the total cross section are shown in Table V. With the introduction of the cuts, the effects of the nonfactorizable corrections become more pronounced. Instead of increasing the cross sections, as was the case in the earlier comparisons (Tables II and III), the cross sections are now decreased by the inclusion of these corrections. The relative size of the off-shell contributions also increases from $\sim 1\%$ to a few percent.

TABLE IV. Input parameters used for calculating the cross sections shown in Table V.

$m_t = 172$ GeV	$M_Z = 91.2$ GeV
$M_W = 80.4$ GeV	$p_T(J_b) > 20$ GeV
$\alpha_{\rm ew} = 0.03394$	$p_T(e) > 25$ GeV
$\Gamma_W = 2.14$ GeV	$\not{E}_T > 25$ GeV
$\Gamma_t^{\rm NLO} = 1.32813$ GeV	$120 < m_{\rm inv} < 200$ GeV

TABLE V. Comparison of leading order and next-to-leading order total cross sections for our minimal realistic setup.

	σ^t	σ^{t^*}
LO (pb)	2.6786(1)	2.519(1)
NLO (pb)	2.3079(1)	2.227(4)

B. Distributions

Partial results for kinematical distributions computed with the method presented here have been shown in Ref. [57]. In this section we will consider the minimal realistic setup described in the previous subsection, and use the parameters and cuts given in Table IV.

The first distribution we present is that of the transverse mass of the top, defined as

$$m_{\rm T}^2 = |p_T(J_b)|^2 + |p_T(e)|^2 + |p_T(\nu)|^2 - (\vec{p}_T(J_b) + \vec{p}_T(e) + \vec{p}_T(\nu))^2. \quad (4.4)$$

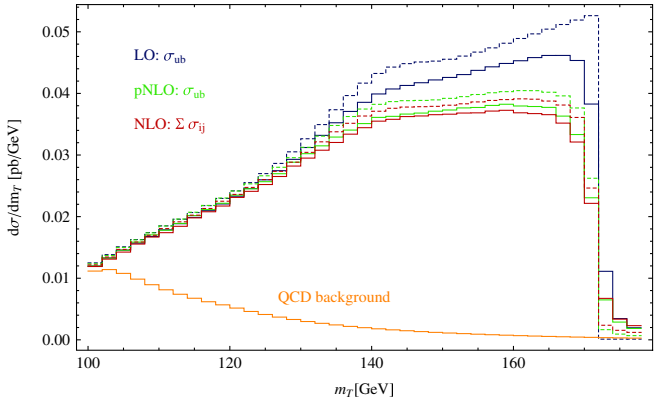

FIG. 4 (color online). Transverse top mass distribution for on-shell (dashed lines) and resonant (solid lines) top-quark production. LO results are shown in blue/dark, pNLO results (see text for explanation) in green/light, and full NLO results in red. The orange line at the bottom shows the subleading QCD contribution.

We will compare on-shell ($ub \to {}^{t}dbW$) and resonant ($ub \to {}^{t^*}dbW$) top-quark production, shown as dashed and solid lines, respectively, in Fig. 4. To assess the importance of higher-order corrections, we will consider LO results (blue); full NLO results (red), including also partonic processes with gluons in the initial state; and partial NLO results (pNLO, green), including only one-loop corrections to partonic processes that are present at LO. Overall, the differences between the on-shell and resonant results are small. However, the off-shell effects do significantly change the shape of the distribution near the boundary $m_{\mathrm{T}} = m_t$. As expected, the LO on-shell distribution shows a sharp edge at this boundary. The on-shell pNLO and NLO results have a contribution for $m_{\mathrm{T}} > m_t$, because the b jet, J_b, can contain gluon radiation; however, this contribution is very small. In the resonant calculation, we get a contribution in the region $m_{\mathrm{T}} > m_t$ even at LO. This contribution is reduced at NLO but is still significantly larger than in the on-shell result.

It can be seen from Eq. (2.8) that there are also terms of higher order in δ in the squared tree-level matrix element. First, there are the interference terms $g_{\mathrm{ew}}^6 2\,\mathrm{Re}(A_{(-1)}^{(3,0)}[A_{(0)}^{(3,0)}]^*)$; second there are the terms proportional to $g_{\mathrm{ew}}^2 g_s^4 |A^{(1,2)}|^2$, commonly referred to as the QCD background; and, finally, there are subleading electroweak corrections $g_{\mathrm{ew}}^6 |A_{(0)}^{(3,0)}|^2$. The former two are $\mathcal{O}(\delta^2)$, whereas the latter is $\mathcal{O}(\delta^3)$. Therefore, parametrically, these terms are beyond our NLO approximation. However, they are a subset of subleading corrections that are very easy to compute and it is useful to compare their numerical importance with respect to the terms of $\mathcal{O}(\delta^{3/2})$. Thus, the QCD background is shown separately in Fig. 4. This contribution is actually important in the region $m_{\mathrm{T}} \ll m_t$, but is insignificant when $m_{\mathrm{T}} \sim m_t$. The subleading electroweak terms of $\mathcal{O}(\delta^2)$ and $\mathcal{O}(\delta^3)$ are very small, and on the scale of Fig. 4 they would show simply as a straight line along the bottom of the plot.

We now move on to look at our second distribution, the sum of the hadronic transverse momenta, defined as

$$H_{\mathrm{T}}(\mathrm{had}) = |p_T(J_b)| + |p_T(J_l)|, \tag{4.5}$$

where J_l is the (non b) jet with the largest transverse momentum. The results are shown in Fig. 5. In this case, the corrections due to the off-shellness of the top are relatively large. The on-shell and resonant results differ by up to 10% in some bins. On average, the difference is approximately 3–4%, in line with the results presented in Table V. We have studied several similar distributions and the effect of the off-shell corrections is typically somewhat smaller than for $H_{\mathrm{T}}(\mathrm{had})$. Again, the QCD background is separately shown in Fig. 5. As for the transverse mass, it is important only at the edge of the distribution, and the subleading electroweak effects are again too small to be shown.

Finally, we turn to the invariant mass of the top, as defined in Eq. (4.3). The upper panel of Fig. 6 shows the result at leading order for our resonant calculation, along with the next-to-leading order results for both the on-shell and resonant calculations. It should be noted that the leading-order on-shell production and decay distribution is a delta function centered at the top mass and so would appear only as a single point at m_t in the figure. Therefore, it has been omitted.

We can see from the figure that the inclusion of NLO effects causes a deviation from the Breit-Wigner shape of the distribution. We also note that there is a visible difference between the NLO distributions obtained via the two methods. This difference is particularly noticeable at invariant-mass values greater than m_t.

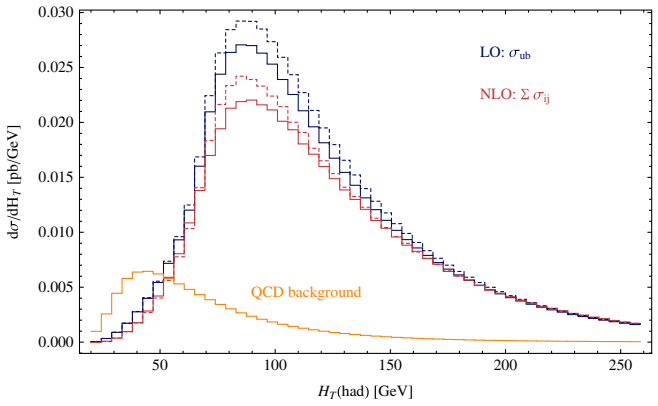

FIG. 5 (color online). H_T(had) distribution for on-shell (dashed line) and resonant (solid line) top-quark production at LO (blue) and NLO (red). The orange line shows the subleading QCD contribution.

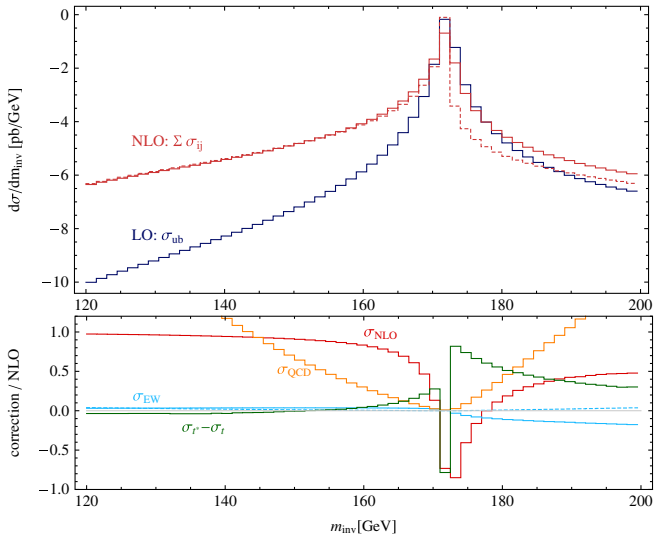

FIG. 6 (color online). Upper panel: Invariant-mass distribution for LO (blue) and NLO (red) resonant-top production, compared to NLO (red, dashed line) on-shell top production. Lower panel: Ratios of various corrections [full NLO correction (red), QCD background (orange), off-shell corrections (green), subleading electroweak corrections (azure)] to the full NLO result.

Considering the shape of the invariant-mass distribution also helps us to understand why the inclusion of off-shell corrections increases the total cross section when no cuts are applied but decreases it when we apply some cuts. At LO, the invariant-mass distribution has a delta-spike shape in the on-shell case but a Breit-Wigner shape in the resonant case. Taking into account NLO corrections, this picture is modified somewhat, but comparing the on-shell and resonant distributions, the former still has a more prominent peak at $m_{\mathrm{inv}} = m_t$, whereas the latter is larger in the region $m_{\mathrm{inv}} > m_t$. Thus, there are two competing effects. If the cut on m_{inv} is mild enough, the increased contribution of the resonant result for $m_{\mathrm{inv}} > m_t$ outweighs the larger peak of the on-shell result, whereas for a tight cut on m_{inv}, the on-shell result is larger.

Note, however, that we must apply a cut to the invariant mass, otherwise our assumption that the top quark is close to resonance is no longer valid and the δ counting no longer applies. As mentioned before, if we take our power counting at face value we would expect our approximation to work in a window of $m_{\mathrm{inv}} - m_t \sim \Gamma_t$. However, the effective theory actually works in a considerably larger window. To illustrate this, let us consider the lower panel of Fig. 6, where we compare the relative importance of the various corrections to the full NLO resonant distribution. The NLO corrections, σ_{NLO} (shown in red), including all corrections of $\mathcal{O}(\delta^{3/2})$, are dominant in the vicinity of $m_{\mathrm{inv}} \simeq m_t$, as expected. They are larger than the $\mathcal{O}(\delta^2)$ QCD corrections, σ_{QCD} (shown in orange), and the subleading electroweak corrections, σ_{EW} (shown in azure). However, away from resonance the formally subleading QCD corrections actually become numerically more important than the formally leading corrections. This is a clear indication that our power counting is no longer applicable in this region and, therefore, the effective theory breaks down. A similar point can be made in the case of the subleading electroweak corrections, which have been divided into $\mathcal{O}(\delta^2)$ contributions (shown as a solid azure line) and $\mathcal{O}(\delta^3)$ contributions (shown as a dashed azure line). These corrections are much smaller than our NLO corrections. In the resonance region, the $\mathcal{O}(\delta^2)$ corrections are larger than the $\mathcal{O}(\delta^3)$ corrections, but for $m_{\mathrm{inv}} \lesssim 130$ GeV this is no longer true. Once more, this indicates the limitations of our power counting in this region. We should also mention that for $m_{\mathrm{inv}} \lesssim 160$ GeV the NLO corrections are huge compared to the LO result and, therefore, our result is not reliable. Finally, the off-shell effects, defined as the difference between the full NLO results for the resonant and on-shell calculations, are shown in green in the lower panel of Fig. 6. These effects are relevant near and above the resonance region, but are very small below resonance.

We stress that the distributions presented here are only a sample of the types of distribution that could be calculated. In principle, any infrared-safe quantity with arbitrary cuts on the final state particles and jets could be easily computed.

V. CONCLUSION AND OUTLOOK

In this work we have presented a method which allows the inclusion of off-shell effects in resonant-particle production with a minimal amount of computation. The method is based on a simultaneous expansion of the cross section in the couplings and the small kinematic variable $\Delta_t/m_t \simeq \Gamma_t/m_t$. It has been applied to t-channel single-top production at the LHC. The calculation includes the first nontrivial corrections to the narrow-width approximation, corresponding to production-decay interference terms, and generalizes earlier results of one-loop corrections to t-channel single-top production.

Generally speaking, off-shell effects are small for inclusive quantities. For the total cross section, for example, we find an effect of the order of 1%. However, depending on the cuts applied, off-shell effects can be sizeable. For most distributions we have considered, the off-shell effects amount to a few percent of the LO result, reaching up to 10% in more extreme cases, such as the H_{T}(had) distribution defined in Eq. (4.5). In particular, they can significantly change the shape of distributions near phase-space boundaries related to off-shell effects, such as the edge for the transverse mass. This is, of course, not surprising since sharp edges in distributions are usually related to having particles on-shell. Thus, allowing the top quark to become slightly off-shell can have a large impact in this region.

The calculation presented here can also be seen as a proof of the workability of the effective-theory method. As we have shown in this paper, the inclusion of the leading off-shell effects is relatively straightforward, requiring in principle only the calculation of simple soft corrections, since the hard part of loop integrals can be easily related to results for on-shell production and decay of the massive particle. Furthermore, the computation of real corrections requires only minor modifications to the standard subtraction procedure. Given the generality of the effective-theory approach, the method can be easily applied to other processes of phenomenological interest at the LHC. One such process is clearly represented by top-quark pair production, which will be intensively exploited for measurements of the top-quark properties, and whose study we reserve for future publications.

ACKNOWLEDGMENTS

We thank F. Giannuzzi for comments on the manuscript. The work of P. F. is supported in part by the ''Premio Morelli-Rotary 2009'' grant of the Rotary Club Bergamo. The work of P. M. is supported by STFC.

[1] T. Aaltonen *et al.* (The CDF collaboration), Phys. Rev. Lett. **103**, 092002 (2009).
[2] V. M. Abazov *et al.* (D0 Collaboration), Phys. Rev. Lett. **103**, 092001 (2009).
[3] J. Alwall *et al.*, Eur. Phys. J. C **49**, 791 (2007).
[4] G. Mahlon and S. J. Parke, Phys. Lett. B **476**, 323 (2000).
[5] P. Motylinski, Phys. Rev. D **80**, 074015 (2009).
[6] W. Bernreuther, J. Phys. G **35**, 083001 (2008).
[7] G. Bordes and B. van Eijk, Nucl. Phys. **B435**, 23 (1995).
[8] T. Stelzer, Z. Sullivan, and S. Willenbrock, Phys. Rev. D **56**, 5919 (1997).
[9] B. W. Harris, E. Laenen, L. Phaf, Z. Sullivan, and S. Weinzierl, Phys. Rev. D **66**, 054024 (2002).
[10] Z. Sullivan, Phys. Rev. D **70**, 114012 (2004).
[11] M. C. Smith and S. Willenbrock, Phys. Rev. D **54**, 6696 (1996).
[12] W. T. Giele, S. Keller, and E. Laenen, Phys. Lett. B **372**, 141 (1996).
[13] M. Beccaria *et al.*, Phys. Rev. D **77**, 113018 (2008).
[14] G. Macorini, S. Moretti, and L. Panizzi, arXiv:1006.1501 [Phys. Rev. D (to be published)].
[15] N. Kidonakis, Phys. Rev. D **75**, 071501 (2007).
[16] A. Denner, S. Dittmaier, and M. Roth, Nucl. Phys. **B519**, 39 (1998).
[17] W. Beenakker, A. P. Chapovsky, and F. A. Berends, Nucl. Phys. **B508**, 17 (1997).
[18] J. M. Campbell, R. K. Ellis, and F. Tramontano, Phys. Rev. D **70**, 094012 (2004).
[19] Q. H. Cao and C. P. Yuan, Phys. Rev. D **71**, 054022 (2005).
[20] Q. H. Cao, R. Schwienhorst, J. A. Benitez, R. Brock, and C. P. Yuan, Phys. Rev. D **72**, 094027 (2005).
[21] J. M. Campbell and F. Tramontano, Nucl. Phys. **B726**, 109 (2005).
[22] R. Pittau, Phys. Lett. B **386**, 397 (1996).
[23] W. Beenakker, F. A. Berends, and A. P. Chapovsky, Phys. Lett. B **454**, 129 (1999).
[24] V. S. Fadin, V. A. Khoze, and A. D. Martin, Phys. Rev. D **49**, 2247 (1994).
[25] K. Melnikov and O. I. Yakovlev, Phys. Lett. B **324**, 217 (1994).
[26] J. M. Campbell, R. Frederix, F. Maltoni, and F. Tramontano, Phys. Rev. Lett. **102**, 182003 (2009).
[27] J. M. Campbell, R. Frederix, F. Maltoni, and F. Tramontano, J. High Energy Phys. 10 (2009) 042.
[28] S. Frixione, E. Laenen, P. Motylinski, and B. R. Webber, J. High Energy Phys. 03 (2006) 092.
[29] S. Alioli, P. Nason, C. Oleari, and E. Re, J. High Energy Phys. 09 (2009) 111; 02 (2010) 11.
[30] R. G. Stuart, Phys. Lett. B **262**, 113 (1991).
[31] A. Aeppli, G. J. van Oldenborgh, and D. Wyler, Nucl. Phys. **B428**, 126 (1994).
[32] M. Beneke, A. P. Chapovsky, A. Signer, and G. Zanderighi, Phys. Rev. Lett. **93**, 011602 (2004).
[33] M. Beneke, A. P. Chapovsky, A. Signer, and G. Zanderighi, Nucl. Phys. **B686**, 205 (2004).
[34] M. Beneke, P. Falgari, C. Schwinn, A. Signer, and G. Zanderighi, Nucl. Phys. **B792**, 89 (2008).
[35] M. Beneke and V. A. Smirnov, Nucl. Phys. **B522**, 321 (1998).
[36] V. A. Smirnov, Springer Tracts Mod. Phys. **177**, 1 (2002).
[37] A. P. Chapovsky, V. A. Khoze, A. Signer, and W. J. Stirling, Nucl. Phys. **B621**, 257 (2002).
[38] E. N. Argyres *et al.*, Phys. Lett. B **358**, 339 (1995).
[39] A. Denner, S. Dittmaier, M. Roth, and D. Wackeroth, Nucl. Phys. **B560**, 33 (1999).
[40] A. Denner and S. Dittmaier, Nucl. Phys. B, Proc. Suppl. **160**, 22 (2006).
[41] F. V. Tkachov, arXiv:hep-ph/9802307.
[42] M. L. Nekrasov, Eur. Phys. J. C **19**, 441 (2001).
[43] M. L. Nekrasov, Phys. Lett. B **545**, 119 (2002).
[44] M. C. Smith and S. S. Willenbrock, Phys. Rev. Lett. **79**, 3825 (1997).
[45] S. Fleming, A. H. Hoang, S. Mantry, and I. W. Stewart, Phys. Rev. D **77**, 074010 (2008).
[46] P. Falgari, Ph.D. thesis, Lehrstuhl für Theoretische Physik E und Institut für Theoretische Physik, 2009, http://darwin.bth.rwth-aachen.de/opus3/volltexte/2009/2682/.
[47] S. Frixione, Z. Kunszt, and A. Signer, Nucl. Phys. **B467**, 399 (1996).
[48] S. Catani and M. H. Seymour, Nucl. Phys. **B485**, 291 (1997); **510**, 503(E) (1998).
[49] Z. Xu, D. H. Zhang, and L. Chang, Nucl. Phys. **B291**, 392 (1987).

[50] M. L. Mangano and S. J. Parke, Phys. Rep. **200**, 301 (1991).
[51] A. Signer and D. Stockinger, Nucl. Phys. **B808**, 88 (2009).
[52] M. Bohm, A. Denner, and H. Joos, *Gauge Theories of the Strong and Electroweak Interaction* (Teubner, Stuttgart, 2001), p. 784.
[53] A. Denner, Fortschr. Phys. **41**, 307 (1993).
[54] F. Jegerlehner and M. Y. Kalmykov, Nucl. Phys. **B676**, 365 (2004).
[55] A. D. Martin, W. J. Stirling, R. S. Thorne, and G. Watt, Eur. Phys. J. C **63**, 189 (2009).
[56] A. D. Martin, R. G. Roberts, W. J. Stirling, and R. S. Thorne, Eur. Phys. J. C **28**, 455 (2003).
[57] P. Falgari, P. Mellor, and A. Signer, Proc. Sci., RADCOR2009 (2010) 013.